

## Key Points:

- We present direct and compelling evidence for the dextral shearing of the Shanxi Graben System
- Dextral strike-slip along the eastern segment of the North Liulengshan Fault (NLSF) is significant in addition to normal faulting
- Late Quaternary dextral strike-slip and vertical slip rates along the eastern segment of the NLSF are both  $\sim 0.2\text{--}0.3$  mm/yr

## Supporting Information:

Supporting Information may be found in the online version of this article.

## Correspondence to:




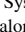



Q. Luo,  
2001111810@stu.pku.edu.cn

## Citation:

Luo, Q., Li, Y., Schoenbohm, L., Rimando, J., Hu, X., Guo, A., et al. (2022). Direct evidence for dextral shearing in the Shanxi Graben System: Geologic and geomorphologic constraints from the North Liulengshan Fault. *Tectonics*, 41, e2022TC007490. <https://doi.org/10.1029/2022TC007490>

Received 3 JUL 2022  
Accepted 16 NOV 2022

# Direct Evidence for Dextral Shearing in the Shanxi Graben System: Geologic and Geomorphologic Constraints From the North Liulengshan Fault

Quanxing Luo<sup>1,2</sup> , Youli Li<sup>1</sup>, Lindsay Schoenbohm<sup>3</sup> , Jeremy Rimando<sup>4</sup> , Xiu Hu<sup>1</sup>, Ailun Guo<sup>1</sup> , Junxiang Zhao<sup>5</sup>, Xinnan Li<sup>2</sup> , Qingri Liu<sup>1</sup> , Shanru Jiang<sup>1</sup>, Chuanyou Li<sup>2</sup> , and Kai Sun<sup>2</sup>

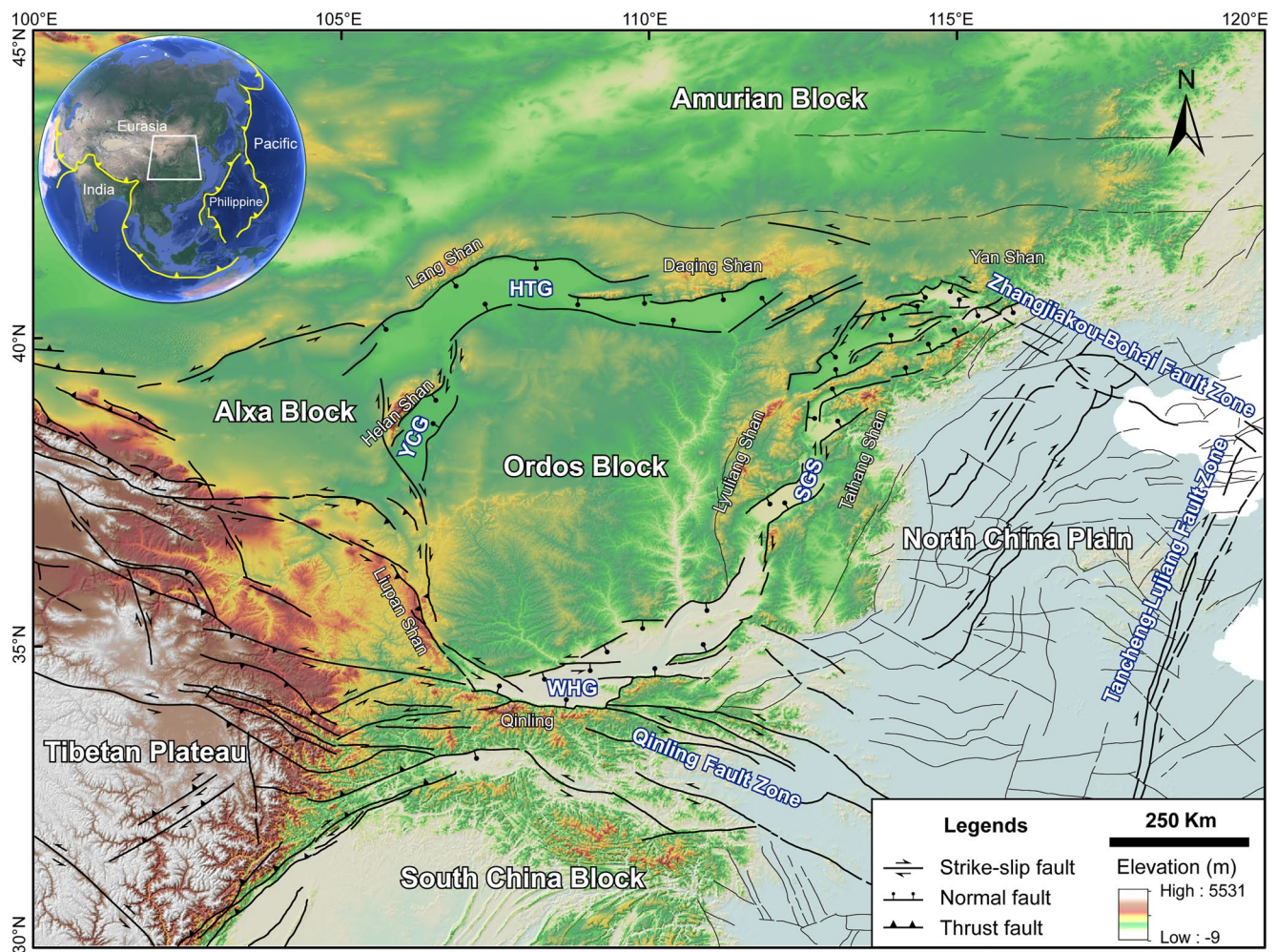
<sup>1</sup>Key Laboratory of Earth Surface Processes of Ministry of Education, Peking University, Beijing, China, <sup>2</sup>State Key Laboratory of Earthquake Dynamics, Institute of Geology, China Earthquake Administration, Beijing, China, <sup>3</sup>Department of Chemical and Physical Sciences, University of Toronto Mississauga, Mississauga, ON, Canada, <sup>4</sup>School of Earth, Environment and Society, McMaster University, Hamilton, ON, Canada, <sup>5</sup>National Institute of Natural Hazards, Ministry of Emergency Management of China, Beijing, China

**Abstract** The Shanxi Graben System (SGS) is one of the first-order Cenozoic tectonic features in North China. Understanding the kinematics of this tectonic system is crucial for deciphering the mechanism of continental rifting and the deformation pattern across North China. Although the SGS has long been thought to be a right-lateral, transtensional shear zone, the geologic and geomorphologic evidence for dextral strike-slip along its internal faults was slim and even controversial. Field investigations, interpretations of satellite imagery, and construction of decimeter-scale digital elevation models from unmanned aerial vehicle surveys were used in this work to investigate the tectonic geomorphology of the eastern segment of the North Liulengshan Fault (NLSF) in the northern SGS. Although this fault segment was previously thought to be a pure normal fault, the presence of geomorphic features such as right-laterally offset terrace risers and gullies, along with an analysis of fault-slip data, suggests a component of right-lateral strike-slip displacement. Combined with optically stimulated luminescence dating of offset fluvial terraces, the late Quaternary right-lateral strike-slip and vertical slip rates of this fault segment are both estimated to be  $\sim 0.2\text{--}0.3$  mm/yr. The discovery of dextral strike-slip along the NLSF provides compelling direct evidence for determining the dextral transtensional kinematics of the SGS. This puts new constraints on our knowledge that the evolution of the SGS is primarily driven by the outward expansion and growth of the Tibetan Plateau and supports the “bookshelf” rotation kinematic model for North China.

**Plain Language Summary** It has long been believed that many right-lateral strike-slip faults may exist in the Shanxi Graben System (SGS) in central North China, but exactly which ones are not fully understood. Here, we report on a newly discovered dextral strike-slip fault—the North Liulengshan Fault in the northern SGS, based on interpretations of historical satellite images and field investigations. The dextral strike-slip motion along the eastern segment of that fault is evidenced by geomorphic features like right-laterally offset terrace risers and gullies and fault striations preserved on exposed fault planes. Combining our displacement measurements and geochronology data yields both right-lateral strike-slip and vertical slip rates of  $\sim 0.2\text{--}0.3$  mm/yr for the fault. This discovery provides key geologic and geomorphic evidence for determining the kinematics of the SGS, which is of great significance for better understanding the geodynamics of the SGS and the deformation pattern of North China.

## 1. Introduction

North China is an ancient craton (i.e., North China Craton) in eastern continental Asia, consisting of two main tectonic blocks, the Ordos Block in the west and the North China Plain in the east (Figure 1; Zhao et al., 2005). Since its formation in the Precambrian, the North China Craton had maintained long-term tectonic stability. However, from the late Mesozoic to the Cenozoic, it has undergone tremendous craton destruction and gradually lost its stability, particularly in its eastern part (Bao et al., 2013; Chen et al., 2009; Jiang et al., 2013; Zhu et al., 2011). As a result of the Indo-Eurasian continental collision and westward subduction of the Pacific Plate, the North China Craton is neotectonically active (Figure 1; Molnar & Tapponnier, 1975; Tapponnier & Molnar, 1977; Northrup et al., 1995; Yin, 2010). Extensive intracontinental rifting (e.g., the circum-Ordos

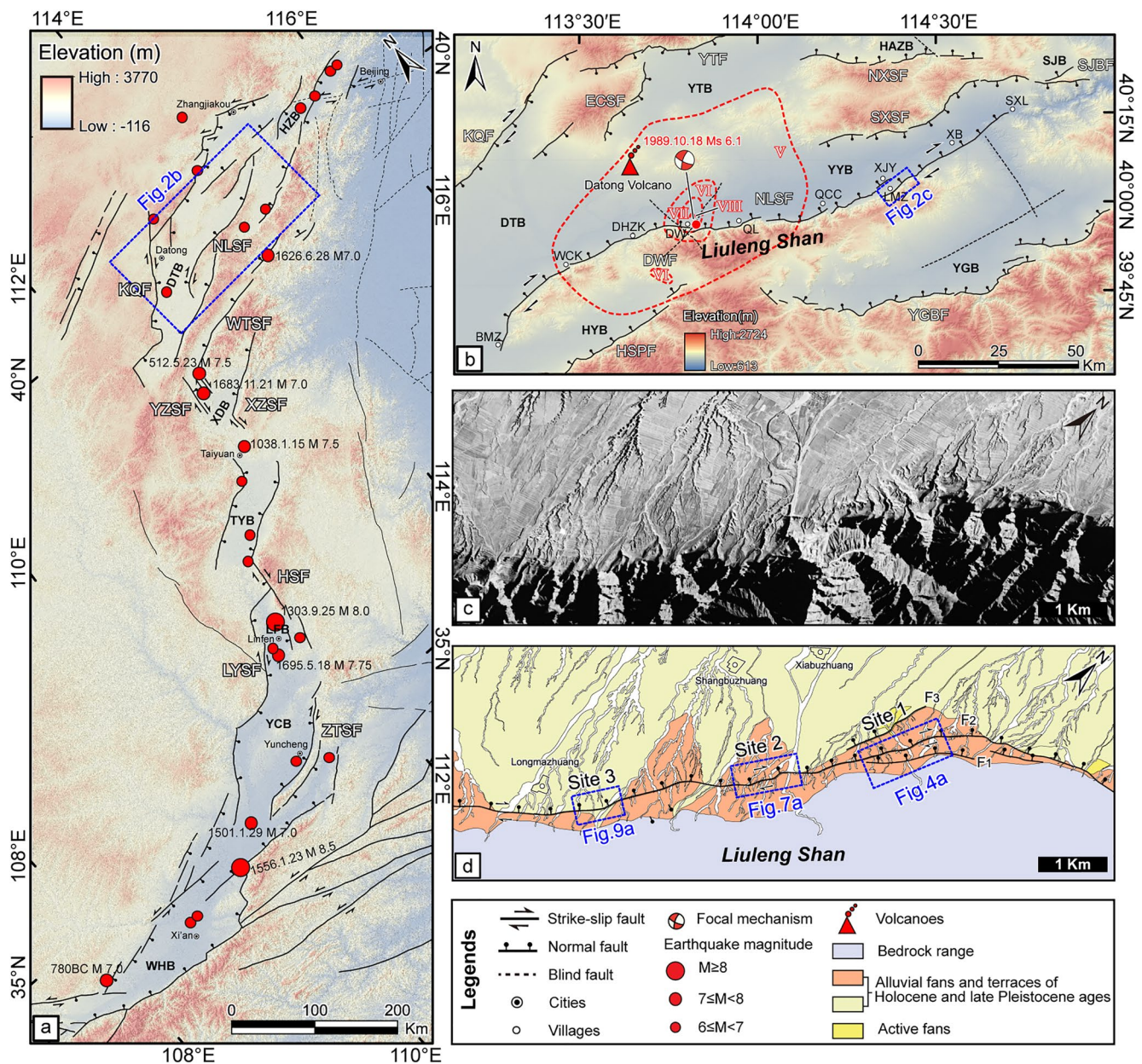


**Figure 1.** Topography and tectonic setting of North China and neighboring regions. Note that the left-stepping en-echelon and sigmoid-shaped geometry of the Shanxi Graben System lying between the Ordos block and North China Plain. Fault data are modified from Deng et al. (2007). Major faults are indicated by thick black lines, while minor and/or inferred faults are represented by lighter, thin lines. Abbreviations: HTG = Hetao Graben, WHG = Weihe Graben, YCG = Yinchuan Graben, SGS = Shanxi Graben System.

graben systems) and intense seismic and igneous activities have made North China one of the most popular sites for geoscientists to explore the mechanism of intracontinental deformation (Clinkscales et al., 2020, 2021; Li et al., 2022; Liu et al., 1983, 2004; Middleton, Walker, Parsons et al., 2016; Middleton, Walker, Rood, et al., 2016; Ren et al., 2002; Zhang et al., 1998, 2016).

The ~1,200 km-long, NE-striking SGS, lying between the stable Ordos Block to the west and the North China Plain to the east, is one of the first-order Cenozoic tectonic features in North China (Figure 1). Understanding the kinematics of this tectonic system has profound implications for deciphering the general mechanisms of continental rifting and the pattern of tectonic deformation in North China. The left-stepping, en-echelon, and sigmoid-shaped geometry of the fault system suggest that the SGS may be a right-lateral, transtensional shear zone (Figure 2a; Li et al., 1998; Xu & Ma, 1992). Although a few earlier Global Positioning System (GPS) observations (e.g., Shen et al., 2000; Yang et al., 2000) dispute this conclusion, the majority of subsequent GPS-based (e.g., Guo et al., 2004, 2022; Hao et al., 2021; Qu et al., 2014; Song et al., 2022; Wang & Shen, 2020; Wang et al., 2011; Zhao et al., 2017), seismological (Li, Kuvvet, et al., 2015; Li, Sørensen, & Atakan, 2015), and paleo-stress studies (Shi et al., 2015) corroborate it. In addition, a set of NNE-striking major basin-bounding faults was interpreted to be responsible for the dextral shearing of the SGS, including from north to south the Kouquan Fault, North Liulengshan Fault (western segment; NLSF), Yunzhongshan Fault, Wutaishan Fault (western segment), Xizhoushan Fault (western segment), Huoshan Fault, Luoyunshan Fault, and Zhongtiaoshan Fault





**Figure 2.** Tectonic setting of the Shanxi Graben System. (a) Topographic map showing Quaternary faults and epicenters of historical earthquakes in the Shanxi Graben System. Faults and earthquakes data are from Deng et al. (2007). (b) Topographic map showing the traces of the North Liulengshan Fault. The red dashed line represents the isoseismic line of the Datong-Yanggao earthquake in AD 1989 based on work by Liu et al. (1992). (c) Satellite image captured in AD 1970 (<https://earthexplorer.usgs.gov/>; last accessed 30 March 2022) and (d) corresponding interpretation showing fault traces of the eastern segment of the North Liulengshan Fault. Abbreviations: HZB = Huaizhuo Basin, DTB = Datong Basin, XDB = Xinding Basin, TYB = Taiyuan Basin, LFB = Linfen Basin, YCB = Yuncheng Basin, WHB = Weihe Basin; HAZB = Huaianzhen Basin; YTB = Yanggao - Tianzhen Basin, SJB = Shenjing Basin, YYB = Yangyuan Basin, HYB = Hunyuan Basin, YGB = Yuguang Basin; KQF = Kouquan Fault, NLSF = North Liulengshan Fault, YZSF = Yunzhongshan Fault, WTSF = Wutaishan Fault, XZSF = Xizhoushan Fault, HSF = Huoshan Fault, LYSF = Luoyunshan Fault, ZTSF = Zhongtiaoshan Fault; YTF = Yanggao - Tianzhen Fault, ECSF = East Cailiangshan Fault, NXSF = North Xiongershan Fault, SXSF = South Xiongershan Fault, SJB = Shenjing Basin Fault, DWF = Dawang Fault, HSPF = Hengshan Piedmont Fault, YGBF = Yuguang Basin Fault; BMZ = Beimazhuang, DHZK = Donghouzikou, DW = Dawang, LMZ = Longmazhuang, QL = Qiulin, QCC = Quchangcheng, SXL = Shixiali, WCK = Wengchengkou, XB = Xinbu, XJY = Xiejiayao.

(eastern segment) (Figure 2a; Deng & Xu, 1995; Deng et al., 1999; Xu & Ma, 1992). However, for a long time, geological and geomorphological confirmation of this expected dextral strike-slip is insufficient or even debatable (Deng & Xu, 1995; Hu et al., 2010; Li et al., 1998; Wang et al., 1996; Xu, 2013; Xu & Deng, 1990; Xu, Ma, et al., 1996; Xu et al., 1986, 2018; Zhang et al., 1998).

For example, based on large-scale geomorphic mapping of the river systems across the faults, Xu et al. (1986) and Xu and Deng (1990) present some evidence for the right-lateral strike-slip along the Xizhoushan Fault and Huoshan Fault. Using offset stream channels as geomorphic markers and  $^{14}\text{C}$  dating method, the authors estimate dextral slip rates of 5.7–7.5 mm/yr for the Xizhoushan Fault and Huoshan Fault over the Holocene. Based on an analysis of offset stream channels using satellite imagery, Zhang et al. (1998) conclude that the Huoshan Fault and Xizhoushan Fault are both right-lateral strike-slip faults. Additionally, some indirect sedimentological evidence for the dextral strike-slip along the Huoshan Fault was presented by Li et al. (1998) and Hu et al. (2010). These authors claim that the dextral movement of the Huoshan Fault caused the juxtaposition of Pliocene gravels with differing lithologies at two locations. However, after an investigation of the planform drainage pattern along the fault, Xu (2013) argues that river deflection along the Huoshan Fault might not be related to the dextral strike-slip. The Hongdong M 8.0 earthquake in AD1303 is one of the few surface-rupturing earthquakes in the SGS and caused about 270,000 fatalities (Figure 2a; State Seismological Bureau, 1988). Studies of the ruptures of this earthquake along the seismogenic Huoshan Fault are not in agreement with the kinematics of the SGS. Xu and Deng (1990) documented a 45-km-long surface rupture zone, with dextral dislocations of 4–8.6 m and vertical throws of ~3.5–5.0 m. On the other hand, a reanalysis of the surface rupture zone by Xu et al. (2018) using high-precision topographic data and field observations, shows that normal sense slip is dominant in both the AD 1303 event and the longer-term, cumulative deformation. Thus, although the Huoshan Fault is one of the most prominent sources of evidence for demonstrating the existence of the dextral strike-slip component of motions in the SGS, the kinematics of faulting remain largely uncertain. The geomorphologic evidence of other dextral strike-slip faults in the SGS is sparse and non-systematic (e.g., Deng & Xu, 1995; Wang et al., 1996; Xu, Ma, et al., 1996). Therefore, more data are needed to understand the importance and significance of purported dextral shearing within the SGS.

In this paper, we present geologic and geomorphologic evidence for the dextral strike-slip along the eastern segment of the NLSF (see Figure 2b for location). Detailed field observations show that dextral strike-slip is evidenced by right-laterally offset fluvial terrace risers, deflected stream channels, and fault striations on fault planes. Our observations provide the first direct and conclusive field evidence for dextral shearing in the SGS, which could help further enrich the understanding of the geodynamics of the SGS and the tectonics of North China.

## 2. Geologic Setting

The SGS, which is located on the east side of the Ordos Block (Figure 1), is one of the most active intracontinental rift systems in the India-Asia collision (Ai et al., 2019; Yin, 2000). From north to south, it consists of a series of grabens arranged in a left-stepping, en-echelon pattern, including from north to south the Huaizhuo, Datong, Xinding, Taiyuan, Linfen, and Yuncheng basins, stretching for 1,200 km, with a width of 60–200 km. (Figure 2a; Li et al., 1998; Xu & Ma, 1992; Xu et al., 1993). The SGS can be geometrically divided into three domains: two broad, ENE-striking extensional zones in the north and south, and a narrow, NNE-striking, right-lateral transtensional zone in the center (Clinkscale et al., 2021; Middleton et al., 2017; Xu & Ma, 1992; Xu et al., 1993). The Qinling mountains and Yan Shan (“Shan” = “mountains” in Chinese) are the southern and northern boundaries of the SGS, respectively (Figure 1). The SGS is sandwiched between Lyuliang Shan to the west and Taihang Shan to the east (Figure 1). The location and geometry of the grabens are partly inherited from the NE-SW striking Taihang-Lyuliang fold belt, formed during the Middle-Late Jurassic - Early Cretaceous Yanshanian orogenic event (Clinkscale & Kapp, 2019; Clinkscale et al., 2020; Xu & Ma, 1992).

Earlier studies suggested that the SGS initiated in the Pliocene as basal deposits in the north and central grabens are primarily of Pliocene age (Li et al., 1998; Xu & Ma, 1992; Xu et al., 1993). Recent low-temperature thermochronology and paleomagnetic studies, however, suggest that rifting of the SGS began in the late Miocene (Bi et al., 2022; Chen et al., 2021; Clinkscale et al., 2020, 2021; Su et al., 2021) and may have propagated northward through time (Ai et al., 2019; Bao et al., 2013; Jiang et al., 2013; Song et al., 2012). Rifting of the SGS is active, manifested by strong earthquakes and the occurrence of Quaternary volcanism within the rift zones (e.g., the Datong Volcano) (Figures 2a and 2b). Since AD 231, there have been at least  $19 M \geq 6$  earthquakes in the SGS (Xu et al., 1993).

Our study area is located in the northern SGS, which is characterized by ENE-striking normal faults and asymmetric half-grabens with footwall blocks tilted to the SSE (and NNW), creating typical basin-and-range morphology



(Luo et al., 2021; Xu & Ma, 1992; Xu et al., 2002). Geodetic surveys indicate that the northern SGS is dominated by horizontal crustal extension at rates of 1–2 mm/yr in the NNW-SSE direction (Middleton et al., 2017; Zhao et al., 2017). The Datong Basin is the largest in the northern SGS. It consists of a series of Pliocene subbasins such as the Yanggao-Tianzhen, Yangyuan, and Hunyuan Basins. (Figure 2b). The latest high-resolution magnetic stratigraphy of the sedimentary sequence indicates that the Datong Basin was developed no later than ca. 7 Ma (Bi et al., 2022). Seismicity in the northern SGS is primarily characterized by moderate earthquakes both in historical and instrumental records (Xu et al., 2002). However, in the eastern part of Datong Basin, an  $M_s$  6.1 earthquake occurred on 18 October 1989, which resulted in a significant amount of casualties and damage, with focal mechanism solutions that show pure right-lateral strike-slip motion (Figure 2b; Li, Kuvvet, et al., 2015; Li, Sørensen, & Atakan, 2015; Zhuo et al., 2019).

The NLSF, which defines the southeastern margin of the Datong Basin and the southern margin of the Yangyuan Basin, is one of the major Holocene active faults in the northern SGS (Figure 2b; Deng et al., 1994; Xu, Nobuyuki, et al., 1996; Yin et al., 1997). It extends for more than 150 km from Beimazhuang village in the southwest to Shixiali village in the northeast, juxtaposing basement rocks of the Liuleng Shan in its footwall against Neogene-Quaternary deposits of the Datong-Yangyuan Basin in the hanging wall (Figure 2b; Duan & Fang, 1995; Xu et al., 2002). The overall strike of the NLSF changes from NE in the southwest to E in the vicinity of Dawang village and then to NE again approximately at Quchangcheng village in the northeast (Figure 2b). The sense of motion of the NLSF has long been the subject of debate, especially along the western segment (i.e., Beimazhuang to Wengchengkou segment). Deng and Xu (1995) and Xu, Ma, et al. (1996) propose that this segment is dominated by right-lateral strike-slip, based on the mapping of offset stream channels. Sun (2018), however, argues for pure dip-slip, normal-sense displacement along the entire NLSF based on field investigations and satellite imagery interpretations. Luo et al. (2022) document dominant right-lateral strike-slip displacement along the western fault segment with only minor normal faulting and the strike-slip and throw rates of approximately  $1.6 \pm 0.3$  mm/yr and 0.2 mm/yr, respectively. However, they base their conclusions only on offset stream channels, lacking other geomorphologic and geologic features like offset terrace risers and fault striations. Except for the western segment, the motion along the rest of the NLSF is thought to behave as purely normal faults, with vertical slip rates ranging from 0.1 to 1.1 mm/yr (Deng et al., 1994; Duan & Fang, 1995; Middleton et al., 2017; Sun, 2018; Xu, Nobuyuki, et al., 1996).

### 3. Methods

#### 3.1. Quaternary Mapping

To map active fault strands and geomorphic surfaces, and to precisely measure offsets, we use a combination of field investigation and inspection of high-resolution satellite images. Our imagery includes Google Earth and old-archived declassified data (<https://earthexplorer.usgs.gov/>), as well as high-resolution topographic data derived from unmanned aerial vehicles (UAV) photogrammetry (e.g., Johnson et al., 2014; Lucieer et al., 2014; Westoby et al., 2012). Historical satellite images can be useful tools for studying strike-slip fault topography in environments with strong artificial modification (Jiang et al., 2017; Kurtz et al., 2018). Human activities including road construction, afforestation, and urbanization have resulted in significant topography changes along the NLSF. Historical remote sensing images can therefore help us identify geomorphic features that have since been obliterated that are characteristic of strike-slip settings, such as linear fault-parallel valleys, elongated/offset/warped stream channels (rivers), laterally offset fluvial terraces, and linear fault scarps in extensional settings. They also allow us to select field sites with no or only minor artificial modifications for further detailed research.

We developed high-resolution digital surface models (DSMs) using the structure from motion technique based on a UAV platform to better highlight the features of each site and measure the offset of displaced geomorphic surfaces. At each location, hundreds of aerial photographs were taken with a DJI Phantom 4 Pro drone from a flight altitude of 100–200 m, with an overlap of 80%. Ground control points were deployed before photograph collecting and incorporated into the modeling process to constrain scale. A Trimble 7X post-processed kinematic differential global positioning system with a 3–5 cm precision was used to geospatially determine the center of each GCP. Utilizing the Agisoft Photoscan software, we obtained 0.2 m resolution DSMs along the fault trace at three locations (Site 1, 2, and 3 in Figure 2d) using the processing workflow protocols of Johnson et al. (2014). Based on the exported DSMs, hillshade, slope, and contour maps were created in ArcGIS and utilized to map the deformed geomorphic features. The height above the modern stream, degree of dissection, height of the fault

**Table 1**  
OSL Dating Results

Sample code	Latitude (°N)	Longitude (°E)	Elevation (m)	Depth (m)	U (ppm)	Th (ppm)	K (%)	Moisture (%)	Dose rate (Gy/ka)	Equivalent dose (Gy)	Age <sup>a</sup> (ka)	Age model <sup>b</sup>	OD <sup>c</sup> (%)
LLS-OSL-15	40.032	114.391	1,135	1.1	2.9 ± 0.04	10.3 ± 0.06	1.82 ± 0.02	6.30	3.21 ± 0.13	82.18 ± 2.61	25.6 ± 1.3	CAM	15.65 ± 2.44
LLS-OSL-16	40.032	114.391	1,134	2.0	2.74 ± 0.03	10.9 ± 0.08	1.9 ± 0.02	9.31	3.16 ± 0.12	115.19 ± 3.55	36.44 ± 1.8	CAM	15.19 ± 2.37
LLS-OSL-18	40.061	114.419	1,062	1.0	3.69 ± 0.12	8.92 ± 0.12	1.25 ± 0.01	9.72	2.67 ± 0.10	127.36 ± 3.86	47.8 ± 2.3	CAM	11.40 ± 2.63
LLS-OSL-20	40.048	114.407	1,067	2.5	1.75 ± 0.01	7.6 ± 0.2	1.66 ± 0.02	4.05	2.66 ± 0.11	40.78 ± 2.69	15.4 ± 1.2	MAM	22.15 ± 3.17

<sup>a</sup>The age uncertainty is 2  $\sigma$ . The dating technique is the single-aliquot regenerative-dose protocol (SAR), and the dating material is quartz. <sup>b</sup>Abbreviations: CAM = central age model, MAM = minimum age model (Galbraith & Roberts, 2012). <sup>c</sup>OD = overdispersion percentage of equivalent dose distribution (at 2  $\sigma$  errors).

scarp/s (if present), and textural differences in imagery data were used to differentiate the alluvial fan units and fluvial terraces by relative age.

### 3.2. Fault Kinematic Analysis

Structural analysis of fault kinematic indicators is an important means to determine fault kinematics (e.g., Benavente et al., 2021; Radaideh & Mosar, 2021). We collected data in the field from exposed bedrock fault planes that exhibited slickensides in three localities along the fault, which consists of dip and dip azimuth of the fault plane and rakes of slickenlines. Given the protracted Cenozoic history of movement along the NLSF, the bedrock fault planes possibly preserve slickenlines from earlier episodes of slip that do not reflect the current fault kinematics. Therefore, we only collected measurements from bedrock fault planes that either offset late Quaternary sediments or bedrock fault planes that are found adjacent to scarps that offset late Quaternary deposits. The slickenline rakes were measured counterclockwise following the right-hand rule for reporting strike direction. Since the fault exhibited a normal component of slip, the rake measurements were all negative (slip vector pointing downward; Table S1 in Supporting Information S1). Typically, for normal fault, slip vectors will have rakes of  $-70^\circ$  to  $-110^\circ$ , specifically,  $-90^\circ$  for pure normal fault; Slip vectors have rakes of  $-110^\circ$  to  $-160^\circ$  usually indicating normal right-lateral oblique-slip fault, while slip vectors with rakes of  $-20^\circ$  to  $-70^\circ$  indicate normal left-lateral oblique-slip fault (Cronin, 2010). Finally, to better express the fault slip sense, the collected fault-slip data were utilized to plot stereonets (focal mechanism solution “beachball” diagrams) employing the FaultKin 8 software (Allmendinger et al., 2012; Marrett & Allmendinger, 1990).

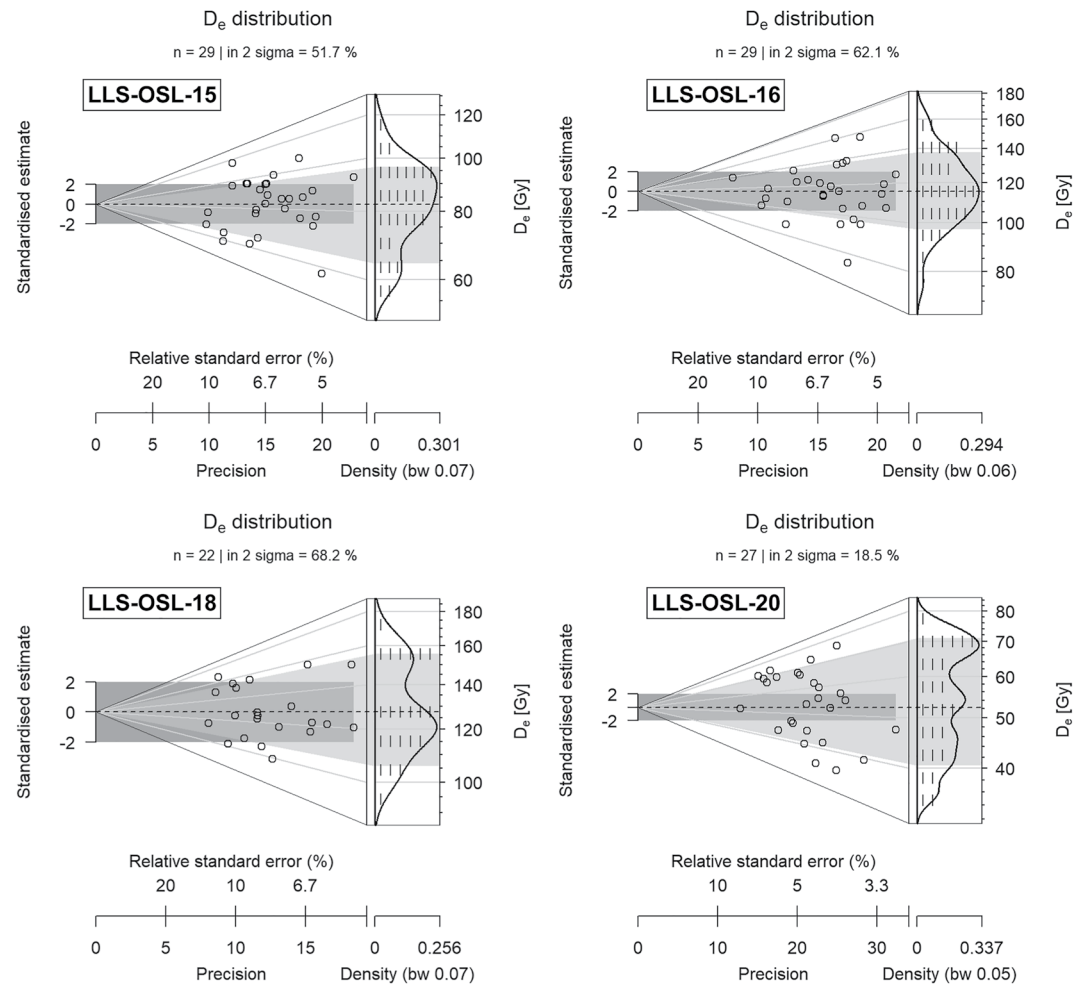
### 3.3. Quaternary Dating

Optically Stimulated Luminescence (OSL) dating, one of the main methods for estimating the depositional age of sediments over the past  $\sim 500$  ka, determines the last time quartz (or feldspar) in sediments was exposed to daylight (Murray et al., 2021). In this study, a total of four OSL samples were collected from terrace deposits and tested to approximate the minimum/maximum abandonment ages (Hu et al., 2021) of the displaced terraces along the NLSF. Stainless steel tubes (25 cm in length and 5 cm in diameter) were hammered into freshly cleaned sections. Once the tubes were filled, they were removed and sealed with aluminum foil, black opaque plastic bags, and immediately wrapped with plastic tape to prevent exposure to sunlight and loss of moisture during transportation and storage. We sampled either fine-grained sand in the terrace alluvium or the overlying loess when no layer of fine-grained sand in the terrace gravel was available. Quartz grains obtained from each sample were measured with the single-aliquot regenerative-dose protocol (SAR) procedure at the Key Laboratory of Crustal Dynamics of the National Institute of Natural Hazards, Ministry of Emergency Management of China, according to the standard procedures of Murray and Wintle (2000, 2003). Further details on the laboratory procedures for the SAR procedure are available in the Supporting Information S1 document. All of the relevant OSL dating results are listed in Table 1. The overdispersion value (OD; expressed as a percentage) is a commonly-used metric to estimate the relative standard deviation from a central equivalent dose ( $D_e$ ) value in context of a statistical estimate of errors (Galbraith & Roberts, 2012). OD values  $\sim \leq 20\%$  are routinely assessed for quartz grains that are well solar reset, while OD values  $> 20\%$  may indicate mixing of grains of various ages or the partial solar resetting of grains. As indicated by the OD values in Table 1 and the centralized distributions of  $D_e$  values (Figure 3), samples LLS-OSL-15, LLS-OSL-16, and LLS-OSL-18 were uniformly bleached, so we finally use the central age model to calculate the ages of these three samples; Sample LLS-OSL-20 (OD =  $22.15 \pm 3.17\%$ ) seems to contain grains that were incompletely bleached before deposition, so we apply the minimum age model to calculate its age (Galbraith & Roberts, 2012).

### 3.4. Offset Measurement and Slip Rate Calculation

Offset fluvial terrace risers are typically linear, sharply defined features, and therefore can serve as excellent piercing points for measuring displacement along faults. It is also relatively easy to determine their ages by dating the flanking terraces (Cowgill, 2007; Gold et al., 2017; Li et al., 2005; Zhang et al., 2007). Therefore, we use the lateral offset fluvial terrace risers wherever possible to identify strike-slip motion and estimate





**Figure 3.** Abanico plots (Dietze et al., 2016) showing equivalent dose distributions of all samples using the central age model (Galbraith & Roberts, 2012).

strike-slip rates. Unfortunately, at Site 3, the displaced terrace riser has been destroyed by anthropogenic factors. At this site, we, therefore, use the stream channel as a geomorphic marker to estimate the slip rate.

We measure vertical offsets of planar geomorphic markers like fluvial terraces by extracting topographic profiles perpendicular to the fault scarps. We select topographic profiles at sites where no significant erosion or degradation was observed and also ensure that the topographic profile has enough length to span and capture the overall trend of the terrace surface. We divide the profiles into three sections for linear fitting: the hanging wall ( $y_h = m_h x + b_h$ ), scarp ( $y_s = m_s x + b_s$ ) and footwall ( $y_f = m_f x + b_f$ ). We use the approach implemented by Thompson et al. (2002) for vertical offset calculations, which are given by the equation:

$$v(x) = (m_f - m_h) x + b_f - b_h, \quad (1)$$

where  $v$  is the vertical offset,  $x$  is the horizontal distance along the profile,  $y$  is the elevation,  $m$ , and  $b$  is the slope and intercept of the hanging wall, scarp, and footwall fitted line, respectively. We measure the lateral components of slip and estimate associated uncertainties from offset terrace risers and stream channels using MATLAB-based software LaDiCaoz\_v2 (Haddon et al., 2016; Zielke & Arrowsmith, 2012; Zielke et al., 2015). This tool, which has been used extensively in lateral offset measurement of strike-slip faults (e.g., Li et al., 2018, 2019; Yu et al., 2021), relies on the cross-correlation of topographic data extracted along two fault-parallel cross-sectional profiles located close to the main fault trace.

Following the approach of Thompson et al. (2002), Rood et al. (2011), Hughes et al. (2018), and Luo et al. (2021), we calculate fault slip rates and their uncertainties by carrying out Monte Carlo simulations in a worksheet-based software package, Oracle Crystal Ball (<https://www.oracle.com/middleware/technologies/crystalball.html>). This was done by assigning each input variable a probability density function that describes the uncertainty in that variable. The variables we considered in the vertical slip rate calculations were the ages of geomorphic surfaces, surface slopes ( $m$  in Equation 1), intercept ( $b$  in Equation 1), and fault position along scarps. For each of the first three variables, we assigned normal probability distribution functions (PDFs) (defined by the mean and standard deviation). For the last variable, we used a trapezoidal PDF to model the fault position within the scarp, assuming that the fault position is most likely between one-half and one-third of the scarp height, measured from the base of the scarp, with the likelihood decreasing to zero at the top and base of the scarp (Hughes et al., 2018; Luo et al., 2021). In the strike-slip rate calculations, the input variables that we considered were relatively simple, involving only lateral offsets and ages of geomorphic surfaces which were all assigned normal distribution PDFs.

## 4. Observations and Results

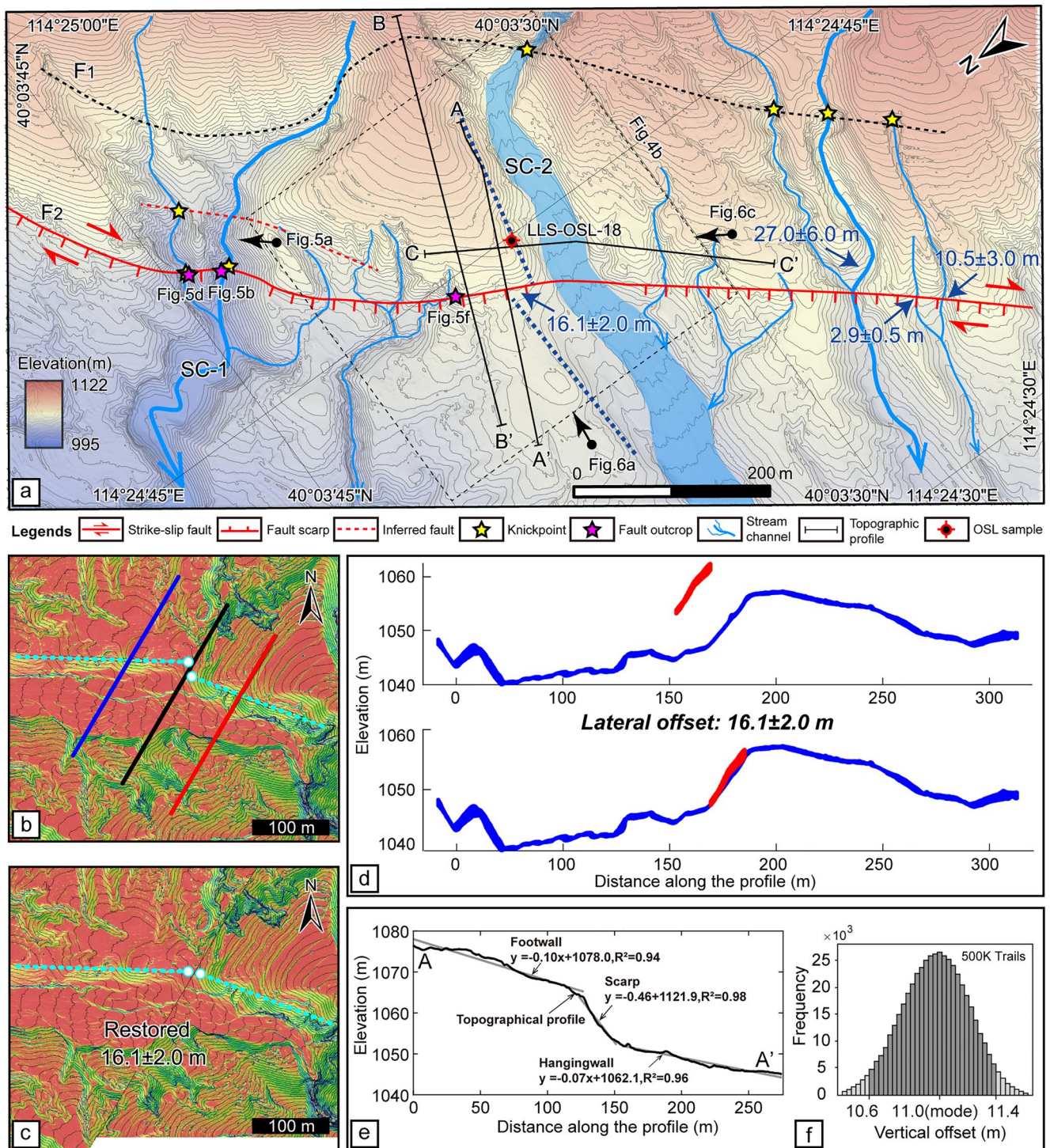
Here we report our field observations on the geomorphic expression of active faulting at three sites which span about 8 km along the eastern segment of the NLSF (Figures 2c and 2d). The general strike of the fault zone is NE 35° and can be traced by its linear imprint on the morphology (Figure 2c). Three fault branches, named  $F_1$  through  $F_3$ , were mapped based on our interpretations of satellite/UAV images and field observations (Figure 2d).  $F_1$  is the southernmost fault branch, which forms a contact between the bedrock range and the Quaternary sediments in the basin, as evidenced by geomorphologic features including linear fault cliffs and knickpoints along the stream channels (Figures 2c, 4a, 6a, and 6d). However, because the linear geomorphic features along  $F_1$  are ambiguous, it is possible that it was inactive throughout the late Quaternary.  $F_2$  is the main fault branch of the fault zone, forming a continuous linear morphology on fan complexes and terraces in the foothills, but also forming contacts between bedrock and Quaternary sediments in some locations (Figure 2d).  $F_3$  is the northernmost fault branch, which extends only ~1 km and strikes in a N-S direction (Figure 2d). Because of the limited length of  $F_3$  and the lack of unambiguous geomorphic markers of fault displacement along  $F_1$ , we focus instead on the tectonic-geomorphic features evident along the main fault trace ( $F_2$ ) in the following section.

### 4.1. Site 1: Xiabuzhuang

Site 1 is around 2 km east of Xiabuzhuang village (Figure 2d). The fault trace ( $F_2$ ) was mapped through the identification of linear fault scarps, right laterally offset stream channels, terrace risers, and a series of fault outcrops (Figure 4a). We made careful field observations on the geomorphic features of SC-1 and SC-2 stream channels along the fault strike (Figure 4a). Stream channel SC-1 is deeply incised, exposing ~30 m of fluvial-lacustrine sand-gravel deposits in the footwall (Figure 5a). At the bottom of this channel, we observed bedrock below the fluvial-lacustrine deposits. Along the main northwest flowing SC-1 channel we observed the fault cutting through this bedrock, forming a polished fault plane dipping to NW 290° with an angle of 50° and a 7 m-high knickpoint along the channel (Figure 5b). In the downstream direction, we found a fault exposure that developed in the Quaternary alluvium, which dips to NW 305° at an angle of 85° (Figure 5c). Along a west-flowing tributary to the main SC-1 channel, we observed a 5 m-high knickpoint (Figure 5d). At the base of this bedrock knickpoint, a bedrock fault plane, dipping NW 307° at an angle of 58°, juxtaposes Paleozoic dolomite against Quaternary sediments (Figure 5e). A series of striations with rakes between –120° and –127° were well-preserved, indicating a right lateral transtensional sense of motion (Figure 5e).

On the southeastern side of the fault, along the flanks of stream channel SC-2, four levels of fluvial terraces (designated  $T_1$  to  $T_4$  from lowest to highest) were preserved (Figures 4a and 6a–6c). The  $T_4$  terrace is composed of ~20 m thick fluvial gravels which mainly consist of dolomite clasts with horizontal stratification and good sorting (Figure 6d). Eolian loess covers the  $T_4$  terrace tread, which thickens as it approaches the bedrock ranges (Figures 6d–6e). The terrace  $T_4$  on the northern bank of stream channel SC-2 exhibits prominent vertical and lateral dislocations (Figures 4a and 6a–6c). Below the fault scarp on the  $T_4$  terrace (Figure 4a), a fault outcrop was observed, consisting of two fault planes with similar geometry, one of which cut through the underlying fluvial gravels and overlying loess and ruptured to the ground surface (Figures 5f and 5g). This gives us confidence that the scarps across the  $T_4$  terrace are due to fault displacement. Using the  $T_4/T_1$  terrace riser as a geomorphic marker and a topographic profile across the fault scarp on the  $T_4$  terrace, we measured a right-lateral offset of





**Figure 4.** Displaced geomorphic features along the fault trace at Site 1. (a) Shaded relief map which is built from UAV surveys, overlain with 2 m-interval contour lines showing the main fault trace of the active fault, right laterally offset terrace riser and deflected stream channels, and the locations of fault outcrops, knickpoints, OSL sample location, and topographic profiles. The black dashed box represents the extent of (b). The blue dashed lines denote the right-laterally displaced terrace risers. (b) Slope map with 1m-contour lines overlay showing the general position of the surface trace (black line) and fault-parallel profile lines on footwall (red line) and hanging wall (blue line), and longitudinal tracing of the crest of  $T_4/T_1$  terrace riser (turquoise dashed lines). (c) Reconstruction of the geomorphic offset based on DSM topography sliced and back-slipped along the fault trace. (d) Swath profiles along red and blue profiles in (b) sampled along the corresponding fault-parallel profile lines and fault-parallel profiles projected onto the fault plane according to the feature slope and shifted by the optimal right-lateral offset. (e, f) Topographic profile of A-A' and corresponding frequency histograms derived from Monte Carlo simulations showing the vertical offset of the  $T_4$  terrace. See (a) for the location of this profile.



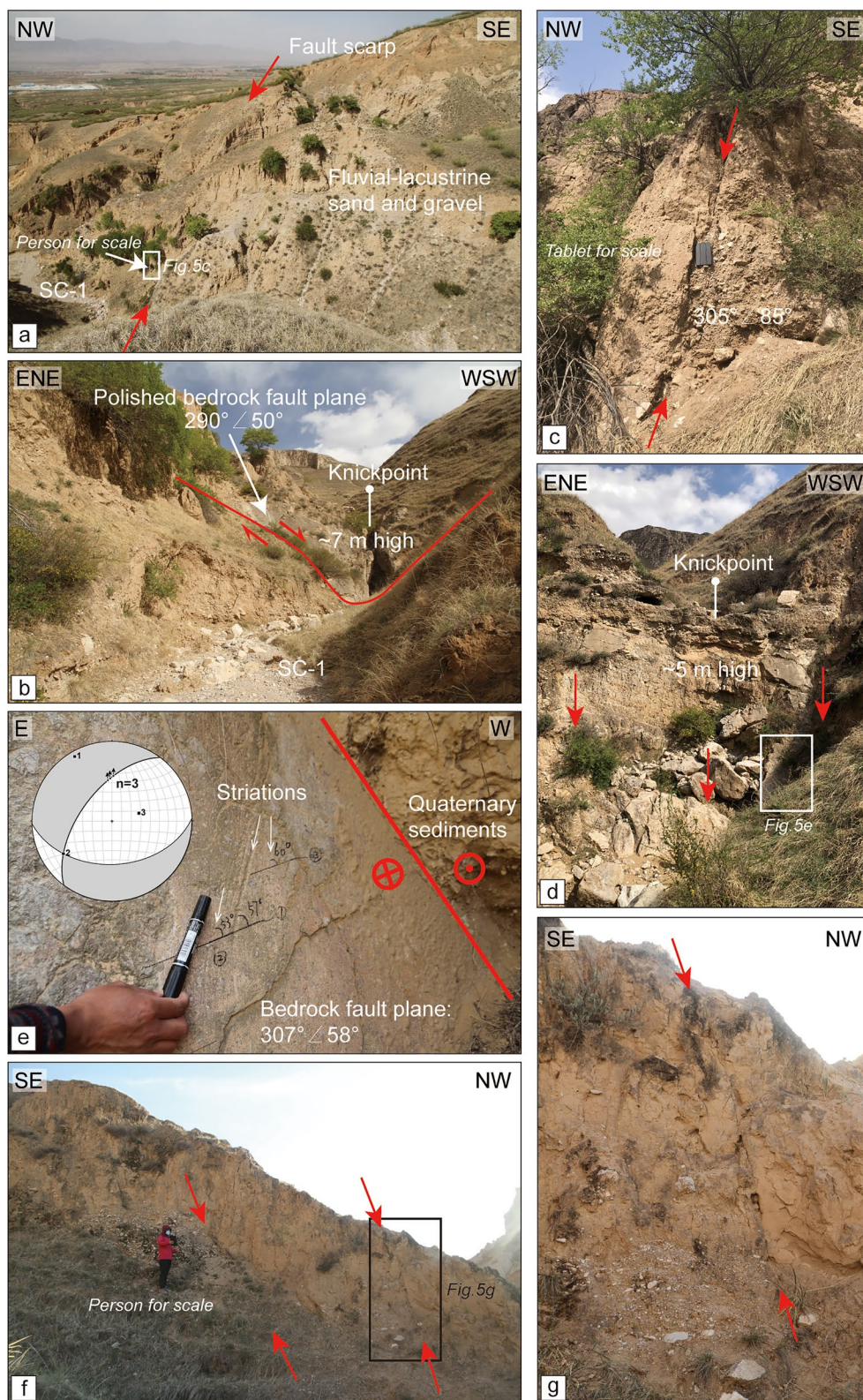
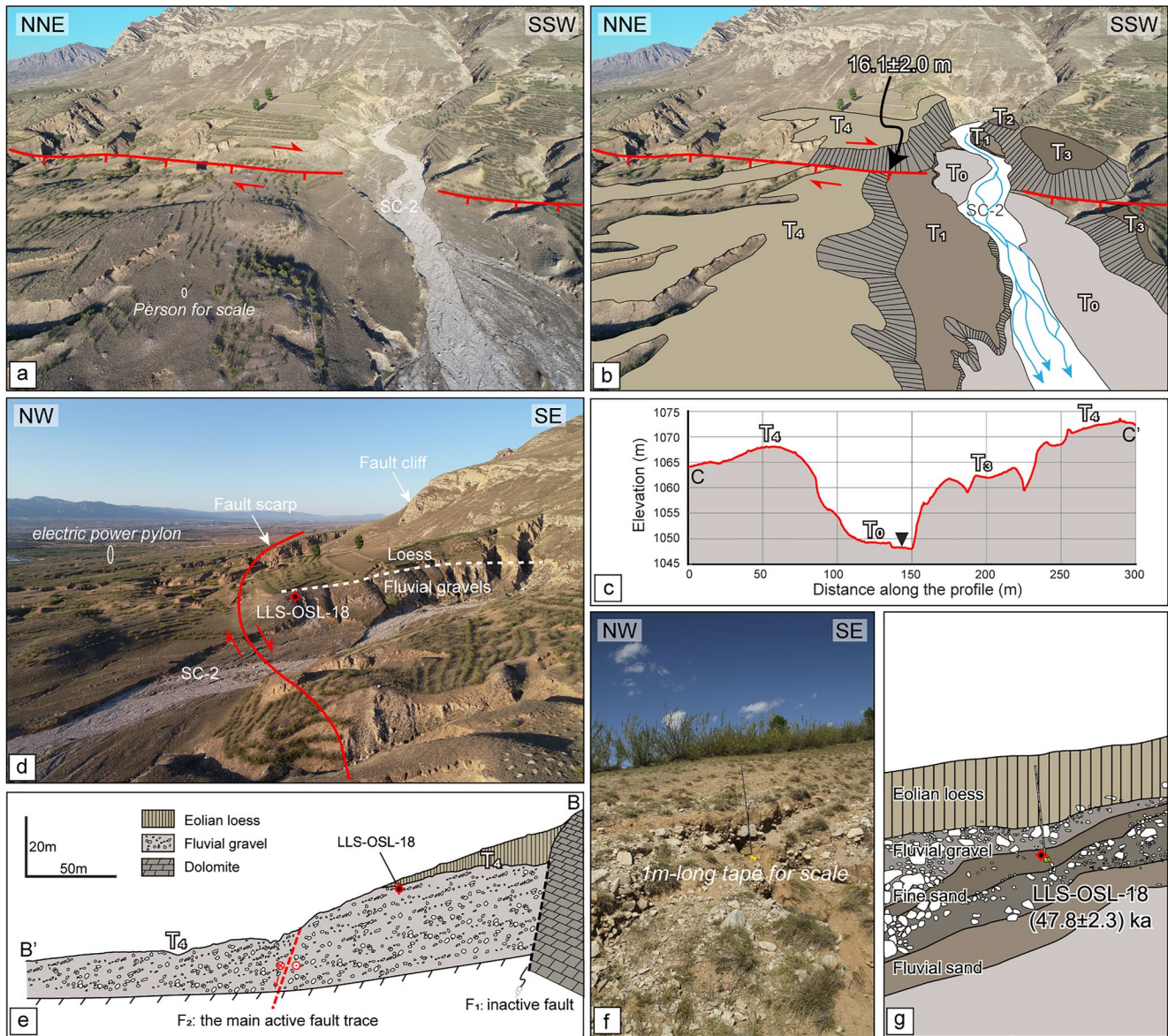


Figure 5.





**Figure 6.** (a) Aerial photo showing displaced geomorphic surfaces along the main fault trace. See Figure 4a for location. (b) The sketch of (a) shows the distribution of fluvial terraces along the SC-2 stream channel. Note that the  $T_4$  terrace has significant vertical and right-lateral offset. (c) Cross-section of stream channel SC-2 showing the terrace staircases. Its location is displayed in Figure 4a. (d) Aerial photo showing displaced geomorphic features and the sedimentary structure of the  $T_4$  terrace. See Figure 4a for location. (e) Longitudinal profile showing the sedimentary structure of the  $T_4$  terrace. The red crosshair represents the OSL sample location. (f, g) Field photo and corresponding interpretation showing the details of OSL sample location.

$16.1 \pm 2.0$  m (Figures 4b–4d, 6b) and a vertical offset of  $11.0 \pm 0.4$  m (95% confidence interval; Figures 4a, 4e, and 4f). Because the downstream terrace on the northern side is likely protected by topography on the upstream side of the fault (Cowgill, 2007; Zhang et al., 2007), the  $T_4/T_1$  terrace riser should begin to accumulate offsets after the abandonment of terrace  $T_4$ . To constrain the abandonment age of terrace  $T_4$ , we collected an OSL sample, LLS-OSL-18, from the fine sand interlayer at the top of the fluvial gravel sediments  $\sim 1$  m below the terrace tread,

**Figure 5.** Field photos showing displaced geomorphic features at Site 1. See Figure 4a for locations. (a) Fluvial-lacustrine sediments with nearly horizontal bedding on the footwall exposed along stream channel SC-1. Red arrows indicate the fault locations. (b) Bedrock exposure and knickpoint at the bottom of stream channel SC-1. (c) Fault plane developed in the Quaternary sediments. (d) Knickpoint along the west-flowing branch of the SC-1 stream channel. (e) Fault striations on the bedrock fault plane indicate a right-lateral transtensional sense of motion. The inset is a stereonet showing slickenside data. Black arrows on the black thick arc (i.e., footwall fault plane) indicate the movement of the footwall with respect to the hanging wall. (f) Fault outcrop below the fault scarps on the  $T_4$  terrace, which cut through the alluvial gravels and overlying eolian loess. (g) A close-up view of (g) shows a fault branch ruptured the ground surface.

which yielded an age of  $47.8 \pm 2.3$  ka (Figures 6d–6g). This age should provide an older bound for the abandonment of the  $T_4$  terrace because there is also  $\sim 0.3$  m-thick fluvial gravel above the fine sand layer sampled. Given this age and the measured offsets, we calculated a right-lateral strike-slip rate of  $0.33 + 0.10/-0.08$  mm/yr and a vertical slip rate of  $0.23 \pm 0.03$  mm/yr for the fault (95% confidence interval).

#### 4.2. Site 2: Shangbuzhuang

Site 2 is located about 3 km southeast of the Shangbuzhuang village (Figure 2d). Active faulting here is expressed by linear fault scarps, fault-parallel valleys, fault troughs, right-laterally deflected stream channels, and terrace risers, as well as well-exposed fault planes along the surface trace of the fault (Figure 7). In the upper reach, the stream channel SC-3 travels from SE to NW, but at the junction with the fault trace, it turns abruptly north and flows subparallel to the fault until it feeds into the Dalongkouyu River (Figure 7a). Several tens of meters wide trough valleys and magnificent bedrock fault scarps, can be seen in the fault-parallel flowing section. These NW-facing bedrock fault planes exposed in this trough have slickenlines with rakes between  $-112^\circ$  and  $-145^\circ$  that indicate right-lateral strike-slip with a considerable normal component (Figures 7b and 7c). We also observed a 6 m-high knickpoint preserved in bedrock on the southeast side at the channel-fault intersection (Figure 7d).

Fault trough valleys with widths of 20–30 m and depths of 6–7 m were also observed on both sides of the SC-4 stream channel which flows from SE to NW, but they extend for less than 100 m (Figure 7e). On the eastern side of a small tributary to the SC-4 channel, a single fault plane dipping to NW  $325^\circ$  at an angle of  $70^\circ$  is exposed (Figures 7a and 7f). The fault plane separates the horizontally bedded fluvial gravels (U3) to the southeast from the fine sand (U1), loess (U2), and gravel (U3) sequence to the northwest; the gravel layer (U3) was offset vertically by about  $4.1 \pm 0.5$  m (Figure 7g). We took an OSL sample at the base of the fine sand layer (U1) on the hanging wall, which yielded an age of  $15.4 \pm 1.2$  ka (Figure 7g). This date provides a minimum age for the accumulation of vertical offset for the U3 gravel layer. As a result, we can estimate a maximum vertical fault slip rate of  $0.26 + 0.09/-0.06$  mm/yr (95% confidence interval). The stream channel SC-4 is right-laterally offset by the fault with an offset of  $26.0 \pm 5.0$  m using its western edge as a piercing point (Figure 7a).

Further to the southwest, a collection of stream channels is consistently deflected dextrally over the fault line, with offsets ranging from a few meters to tens of meters (Figures 7a and 8e). These offset streams are also visible in Figure 8a, a historical satellite image taken in AD 1970 that shows the area before human activities like tree-planting and farm-building altered it. Two levels of terraces ( $T_4$  and  $T_3$ ) on the southwest flank of stream channel SC-5 (Figures 8a, 8b, and 8f) also exhibit right-lateral fault displacement. Using an SfM-derived DSM, we measured lateral offsets of  $22.5 \pm 5.0$  m and  $33.8 \pm 8.0$  m for the  $T_3/T_2$  and  $T_4/T_3$  terrace risers, respectively (Figures 8c and 8d).

#### 4.3. Site 3: Longmazhuang

In the vicinity of Longmazhuang village (Site 3; Figure 2d), the NLSF (or  $F_2$  trace) manifests itself as a NE-striking morphological lineament along the range front (Figures 9a and 9b). Four levels of fluvial terraces ( $T_1$  to  $T_4$  from lowest to highest) are developed and preserved along both flanks of stream channel SC-6, with the  $T_2$  terraces being the most widely distributed (Figures 9a and 10a). The fault passes across the  $T_2$  terrace, forming a characteristic linear surface morphology that can be seen in both the DSM hillshade image and the historical satellite photographs (Figures 9a–9c). The fault right-laterally displaced the edge of the  $T_2$  terrace along the stream channel SC-6 and stream channel SC-7, which is incised into the  $T_2$  terrace, with nearly equal offset magnitudes (Figure 9c). However, the geomorphic marker of the dextral offset of the  $T_2$  terrace was not well-preserved and was obliterated by road-building activities (Figure 9a). Fortunately, the stream channel SC-7 appears to be unmodified by humans and in its original state (Figures 10a and 10b).

We conducted a UAV survey and created a high-resolution DSM to investigate these deformed geomorphic features. Using the LaDiCaoz\_v2 software, we measured a right-lateral offset of  $6.7 \pm 1.0$  m for the stream channel SC-7 using the channel thalweg as a marker (Figures 9d–9f). In addition, we extracted two topographic profiles across the fault scarp on the  $T_2$  terrace that gave vertical offsets of  $6.6 \pm 0.2$  m and  $5.1 \pm 0.2$  m, respectively (Figures 9a and 10d). We consider that the measurement of  $6.6 \pm 0.2$  m is more representative of vertical displacement since the abandonment of the  $T_2$  terrace, although it is a minimum value because we ignore any younger sediment deposition in the hanging wall. The fault is exposed in a pit dug perpendicular to the fault scarp



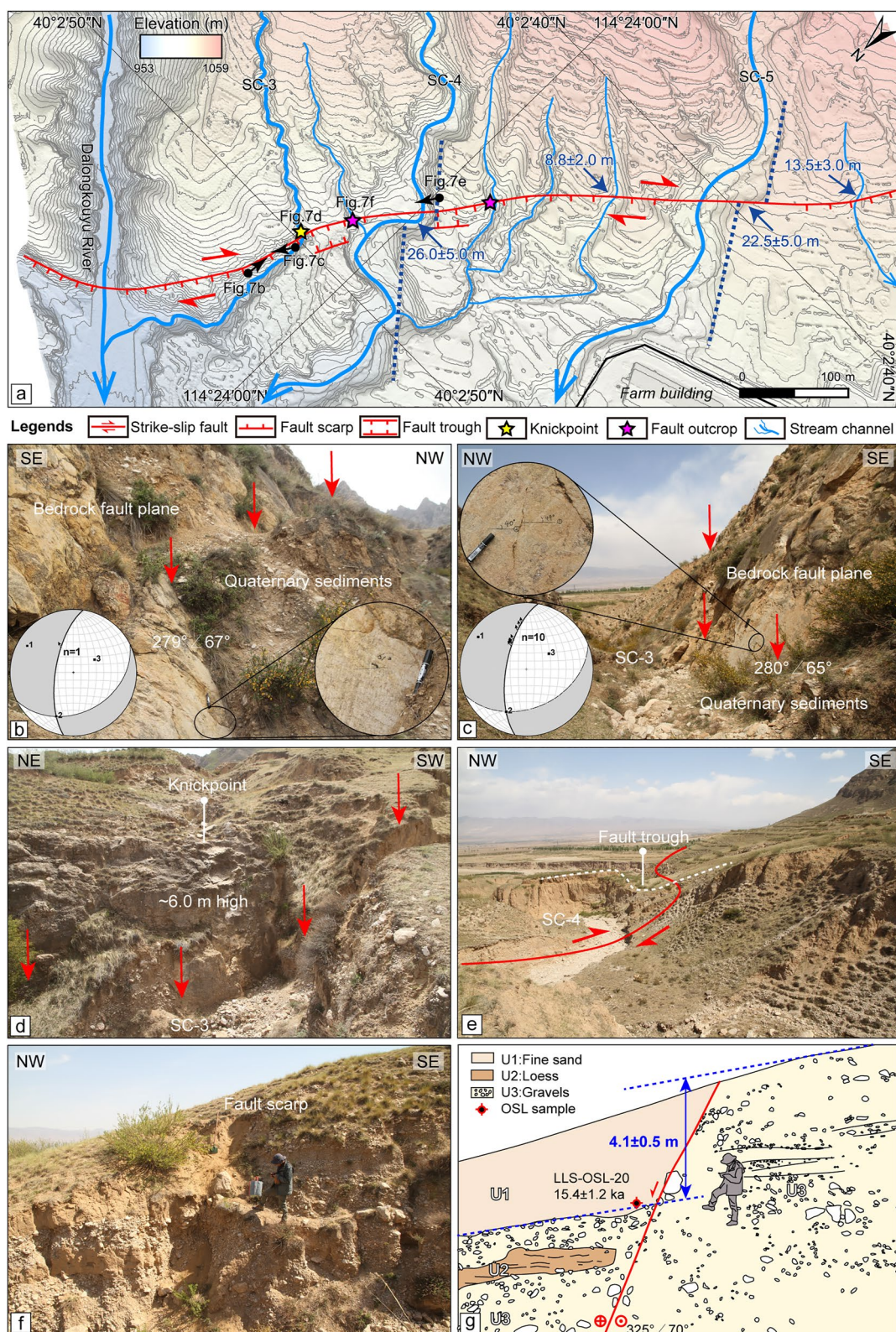


Figure 7.

on the  $T_2$  terrace between the SC-6 and SC-7 stream channels (Figures 9a and 10a). A NW-dipping deformation zone separates fluvial gravels in the footwall from loess in the hanging wall, as revealed by the pit (Figure 10c). Gravels are aligned parallel to the fault plane, which is overlain by the eolian loess. This outcrop provides further compelling evidence that the scarps and lateral offset we observe on the  $T_2$  terrace are products of faulting.

Because stream channel SC-7 has cut through terrace  $T_2$  produced along the stream channel SC-6, its age is expected to be younger than the abandonment age of terrace  $T_2$ . The age of terrace  $T_2$  would give a maximum age for the displacement of stream channel SC-7 (Li et al., 2009). We collected two OSL samples (LLS-OSL-15 and LLS-OSL-16) to constrain the abandonment age of the  $T_2$  terrace (Figure 10e). The LLS-OSL-15 was taken from the base of the eolian loess overlaying the alluvial gravels of the  $T_2$  terrace, while the LLS-OSL-16 was collected from an alluvial sand layer approximately 2.0 m below the terrace tread (Figures 10f and 10g). These yielded ages of  $25.6 \pm 1.3$  ka and  $36.4 \pm 1.8$  ka, respectively, which provides constraints on the interval of time in which the  $T_2$  terrace was likely abandoned. Although the sample OSL-LLS-15 is closer to the top of the fluvial gravel layer (i.e., the abandonment of terrace due to river incision), it cannot be determined whether there is a sedimentary discontinuity after the gravel deposition and before the loess deposition; while OSL-LLS-16 is located more than 1.0 m below the top of the fluvial gravel layer, it may be significantly older than the abandoned age of the terrace. So, we calculate simple arithmetic mean of  $31.0 \pm 2.2$  ka (95% confidence interval) for these two ages, which we use to represent the formation of the  $T_2$  terrace and to determine fault slip rates. Dividing the vertical offset of  $6.6 \pm 0.2$  m and right-lateral offset of  $6.7 \pm 1.0$  m, we estimate a vertical slip and right-lateral strike-slip rates of  $0.21 \pm 0.02$  mm/yr and  $0.21 + 0.07/-0.06$  mm/yr (95% confidence interval), respectively.

## 5. Discussion

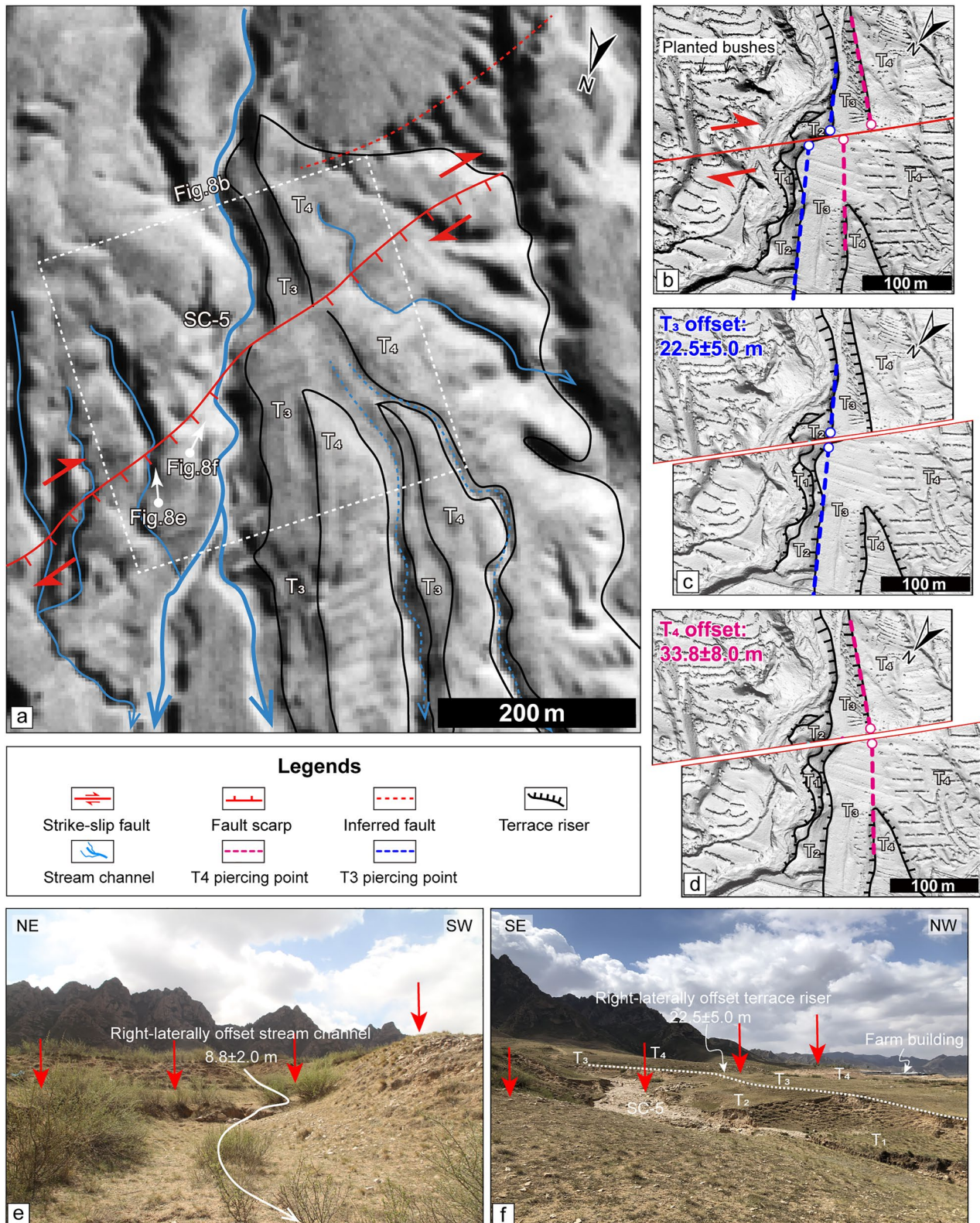
### 5.1. Fault Kinematics of the Eastern Segment of the North Liulengshan Fault

High-resolution SfM-derived DSMs and historical satellite images have provided an opportunity to examine the geomorphic expression of displacement along the NE-striking eastern segment of the NLSF in detail. In contrast to previous conclusions that the eastern segment of the NLSF behaves as a pure normal fault (Deng et al., 1994; Duan & Fang, 1995; Sun, 2018; Xu, Nobuyuki, et al., 1996), we argue that, in addition to normal faulting, the eastern fault segment also has a right-laterally strike-slip component. The presence of linear fault-parallel valleys and troughs, as well as right-laterally offset fluvial terrace risers and stream channels, demonstrates this. Right-lateral displacement is further evidenced by fault striations found at several localities in this work (with rakes ranging from  $-112^\circ$  to  $-145^\circ$ ; Table S1 in Supporting Information S1) and some earlier publications (e.g., Deng et al., 1994; Middleton et al., 2017; Shi et al., 2015). In support of our observations, seismological studies show that the 1989 Datong-Yanggao Ms 6.1 event is characterized by a right-lateral sense of slip and the source of the event may be the NE-striking blind Dawang Fault (Figure 2b; Wang & Wang, 1992; Wei et al., 1992; Zhuo et al., 2019). The eastern segment of the NLSF runs parallel with the Dawang Fault (Figure 2b), so both faults would likely experience the same dextral strike-slip since the current regional stress regime does not have much difference within the range of about 50 km apart (Middleton et al., 2017). The fault motion identified by geologic and geomorphologic evidence thereby is compatible with the tectonic stress state in the northern SGS.

Interestingly, the bulk of fault striations we examined suggests that the normal slip component is slightly larger than the strike-slip component (Figures 5e, 7b, and 7c). For example, the ratio of dip-slip to strike-slip motion is about 1.3–1.7 at Site 1 and it ranges from 0.7 to 2.2 at Site 2 (Table S1 in Supporting Information S1). However, our measurements of the offset terrace risers indicate the opposite, that is, the strike-slip component is slightly larger than the normal faulting component (e.g., Site 1), or they are almost equal (e.g., Site 3). The mismatch can be explained by the following reasons. First, it is still possible that the fault striations correspond to earlier events under a previous stress regime, although these bedrock fault planes show evidence of offsetting late Quaternary

**Figure 7.** (a) Shaded relief map which is built from UAV surveys, overlain by 2 m-interval contour lines showing the mapped fault trace and displaced geomorphic features at Site 2, including linear fault scarps, fault-parallel valleys, right-laterally deflected stream channels, terrace risers, fault outcrops, and knickpoints. See Figure 2d for location. (b, c) Striations preserved on the northwest-facing bedrock fault planes in the fault-parallel valley indicate a right-lateral transtensional sense of motion. Black arrows on the black thick arc (i.e., footwall fault plane) indicate the movement of the footwall with respect to the hanging wall. (d) Field photo showing a knickpoint preserved along the stream channel SC-3. (e) Field photo showing the right-laterally offset stream channel SC-4 and fault troughs on the northeastern side of the channel. (f, g) Field photo and corresponding interpretive sketch showing a fault outcrop observed along a tributary to channel SC-5. The location for (b–g) is indicated in (a).





**Figure 8.** (a) A historical satellite image showing the fault trace and right-laterally deflected stream channels and fluvial terraces. The white dashed box denotes the locations of (b–d). (b) DSM hillshade image derived from UAV photogrammetry showing the distribution of fluvial terraces on the southwestern flank of stream channel SC-5. (c) Reconstruction of the offset observed on the crest of the  $T_3/T_2$  terrace riser. (d) Reconstruction of offset observed on the crest of the  $T_4/T_3$  terrace riser. (e) Field photo showing a right-laterally displaced stream channel. See (a) for its location. (f) Field photo showing the displaced geomorphic features along the stream channel SC-5. The white dashed line denotes the crest of the riser separating terraces  $T_3/T_2$ . See (a) for its location.



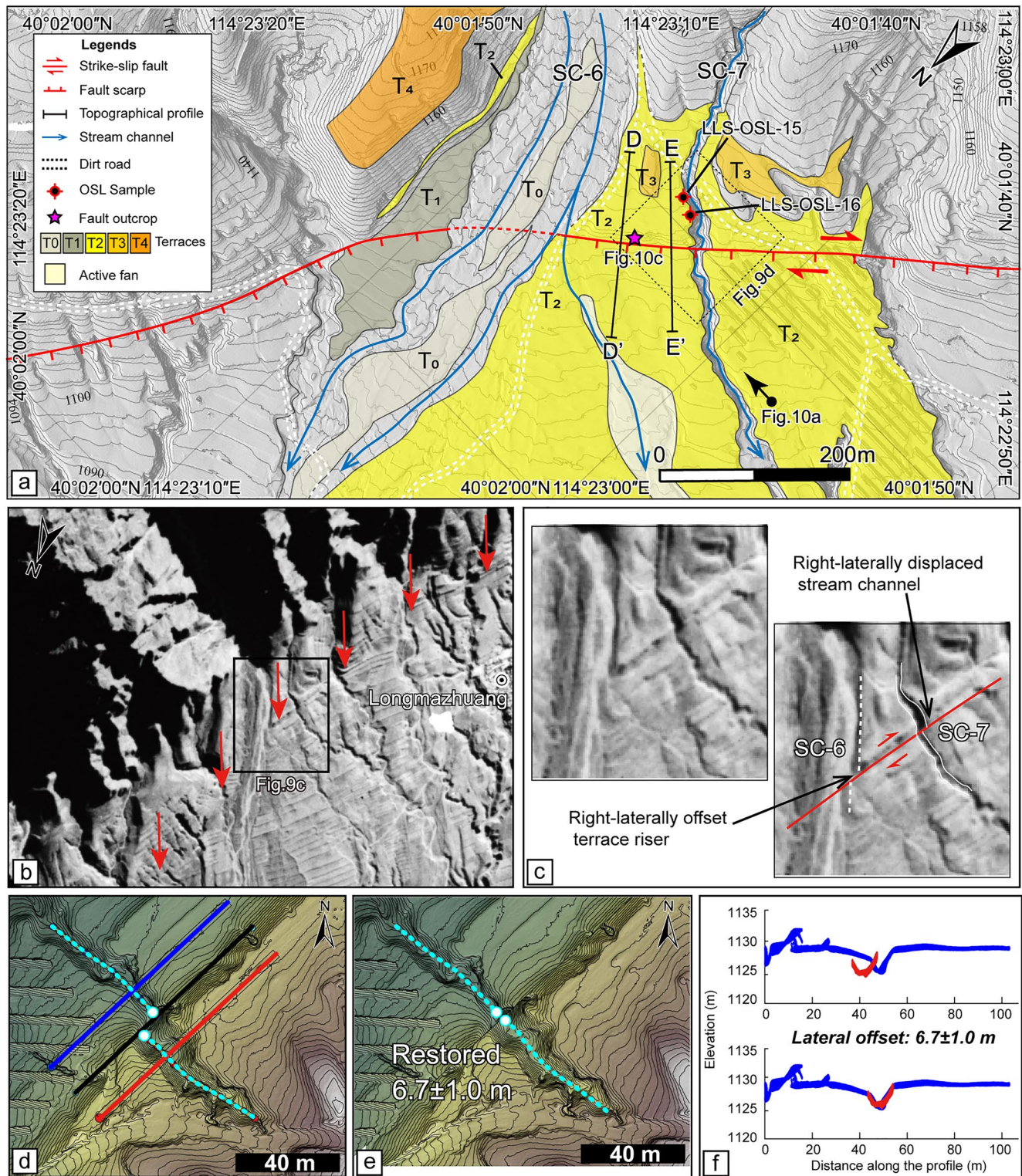
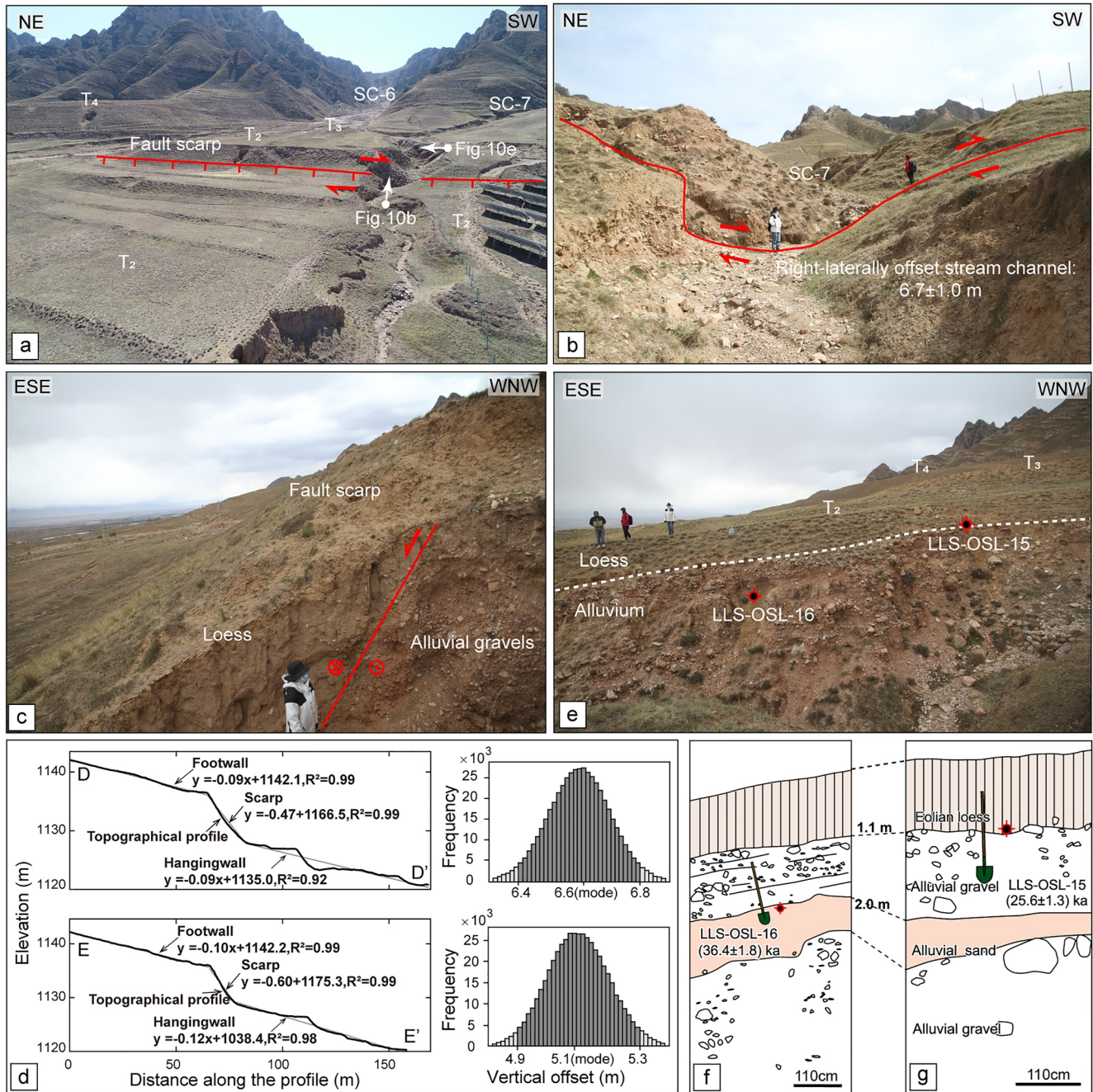


Figure 9.

sediments. The tectonic stress regime of the SGS was not fixed and instead changed over time (Shi et al., 2015). For example, through fault kinematic analysis, Shi et al. (2015) define a three-stage tectonic stress regime over the late Miocene related to the northeastward growth of the Tibetan Plateau. Chen et al. (2015) document that the Yangyuan Basin experienced a three-stage evolution related to tectonic factors during the late Cenozoic based





**Figure 10.** (a) Aerial photo showing the general topography of Site 3. See Figure 9a for its location. (b) Field photo showing the right-lateral displaced stream channel SC-7. (c) Field photo of an exposed fault profile. (d) Topographic profiles and frequency histograms show the vertical offsets of the  $T_2$  terrace. (e) Field photo showing the sample locations and their relationships to the general stratigraphy. Crosshairs denote the sample locations. (f, g) Sketches showing the details of sample locations.

**Figure 9.** (a) DSM hillshade map which is built from UAV surveys, overlain by 2 m-interval contour lines showing the active fault trace and distribution of fluvial terraces at Site 3. See Figure 2d for location. (b) Old archived satellite image illustrating the linear morphology of the mountain front. (c) A historical satellite image showing the original state of the displaced geomorphic features. Note that the edge of the terrace and the stream channel cut through the terrace were right-laterally displaced by the fault. (d) Topographic map overlain by 1 m-contour lines, which shows the general position of the fault trace (black line), fault-parallel profile lines on the southeast uplift footwall (red line) and northwest down hanging wall (blue line), and longitudinal tracing along the thalweg of stream channel SC-7 (turquoise dashed lines). (e) Reconstruction of the geomorphic offset based on the DSM topography which was sliced and back-slipped along the fault trace. (f) Swaths of red and blue elevation points sampled along the corresponding fault-parallel profile lines and fault-parallel profiles projected onto the fault plane according to the feature slope and shifted by the optimal right-lateral offset.



on sedimentary facies and provenance analysis on basin sediments. So, the kinematics of the NLSF, including the proportion of strike-slip to dip-slip, may also change in tune with the tectonic stress regime. For this reason, we suggest that offset geomorphic features can better characterize the recent fault slip behaviors and that the dextral strike-slip component of the fault should be slightly larger than or about equivalent to the normal faulting component of the fault. Second, the mismatch can be related to the possible pitfalls of measuring displacement. The vertical offset measurements in this work ignore the effect of erosion and accretion of the hanging wall and footwall (Yang et al., 2018). For lateral offset measurement, we use terrace riser crest and stream channels as markers. However, several critical factors can influence the lateral offset measurement, including the erosion of the terrace riser crest, the distance over which a feature is projected into the fault zone, the sinuosity of the stream channel, etc. (Gold et al., 2017; Zielke et al., 2015).

Because the three study sites in this work are closely spaced (only 2 km apart) and there are no geometric discontinuities between them (Figure 2d), they should have similar fault slip histories and thus slip rates. However, we note that the lateral offset magnitudes of the  $T_4$  terrace at Site 2 are nearly twice the cumulative dextral offset of the  $T_4$  terrace at Site 1. Although we labeled them as  $T_4$  terraces, they are most likely not contemporaneous geomorphic features. Due to a lack of suitable materials for OSL dating, we were unable to gather chronological samples from the terraces at Site 2. Nevertheless, estimations of right-lateral strike-slip rate range from  $0.21 \pm 0.07/-0.06$  mm/yr at Site 3 to  $0.33 \pm 0.10/-0.08$  mm/yr at Site 1, and vertical slip rates at all three locations are nearly undistinguishable at 0.21–0.26 mm/yr.

## 5.2. Implications for the Kinematics of the Shanxi Graben System

A review of previously published literature reveals that the geomorphic evidence of dextral shearing in the SGS is only offset streams or rivers, almost without exception (e.g., Deng & Xu, 1995; Wang et al., 1996; Xu & Deng, 1990; Xu, Ma, et al., 1996; Xu et al., 1986; Yu et al., 2020; Zhang et al., 1998; Table S2 in Supporting Information S1). We admit that offset stream channels can be excellent geomorphic markers and have long been used to identify the sense of slip and study the fault slip rate of strike-slip fault systems (e.g., Li et al., 2009; Sieh & Jahns, 1984; Tian & Lin, 2021; Wallace, 1949, 1968). However, continued fault slip often leads to stream capture, which reduces or skews the interpretation of the sense of motion, offset magnitude, and slip rate (Duvall & Tucker, 2015; Fu et al., 2005; Harbert et al., 2018; Huang, 1993; Lacassin et al., 1998; Walker & Allen, 2012). In addition, the initial landform (e.g., initial drainage pattern) and surface processes (i.e., erosion, transportation, and deposition) can also influence the creation and maintaining the fault offsets of stream channels (Harbert et al., 2018; Huang, 1993; Li et al., 2021; Reitman et al., 2019). Moreover, these factors are often superimposed, so it may mislead us if we only use offset streams as indicators of strike-slip faulting.

In this paper, we reported geomorphic and geologic features that support right-lateral strike-slip along the eastern segment of the NLSF including right-lateral offset terrace risers, right-lateral deflected stream channels, and also fault striations. In addition, the presence of linear fault scarps, knickpoints, and fault kinematics analysis also demonstrates the normal faulting component. All of these geologic and geomorphologic evidence corroborate the argument for dextral transtensional movement along the eastern segment of the NLSF. Combined with geodetic observations (e.g., Gao et al., 2022; Hao et al., 2021; Song et al., 2022; Wang & Shen, 2020; Zhang et al., 2018; Zhao et al., 2017), seismological studies (e.g., Li, Kuvvet, et al., 2015; Li, Sørensen, & Atakan, 2015), and fault kinematic analysis (e.g., Shi et al., 2015), we believe that the SGS behaves as a dextral transtensional shearing zone. Considering the challenges of locating well-preserved geomorphic markers and properly measuring vertical and lateral displacements on these, amidst the rapid urban development in recent decades which can erase the fault activity records, our study provides valuable, direct, and compelling evidence for the dextral transtension movement in the SGS, which is critical for determining the kinematics and tectonic framework of the SGS.

Previously, the northern SGS has been thought to be an extensional tectonic domain formed at the end of the transtensional central segment of the SGS, and therefore all ENE-striking faults were believed to behave as pure normal faults, including the NLSF, Yanggao-Tianzhen Fault, and the North and South Xiongershan Faults (Figure 2b; Xu & Ma, 1992; Xu et al., 1993). This school of thought was also previously supported by geodetic observations (e.g., Middleton et al., 2017; Shen et al., 2000; Zhao et al., 2017). However, the abundance of evidence of right-lateral strike-slip along the eastern segment of the NLSF supported by our study demonstrates that the northern SGS exhibits more complex fault kinematics than previously recognized. Field observations and high-resolution topographic data interpretations also show that the western segment of the NLSF is dominated

by right-laterally strike-slip, albeit it is only evidenced by systematically offset stream channels at present (Deng & Xu, 1995; Luo et al., 2022; Xu, Ma, et al., 1996). It is also worth noting that right-lateral displacement on the NE-striking western and eastern segments of the NLSF (arranged in right-stepping, en-echelon style) will form a releasing bend along the EW-striking middle segment of the fault (Figure 2b), where shows no geomorphic evidence of lateral strike-slip based on our and other researcher's observations (e.g., Deng et al., 1994; Duan & Fang, 1995; Xu, Nobuyuki, et al., 1996); Future studies should focus on the partitioning and transfer of tectonic strain across these fault segments. The Kouquan Fault is another major fault in the northern SGS that is previously thought to be a right-lateral strike-slip fault, with slip rates of 0.8–3.6 mm/yr (Figure 2b; Ding & Lu, 1983; Li et al., 2013; Wang et al., 1996). Active fault investigations in recent years, for instance, by Xu et al. (2011), claim that there is hardly convincing evidence for dextral strike-slip. However, assuming that the dextral strike-slip of the Kouquan Fault is real, then combinedly, the western and eastern segments of the NLSF form a roughly 100 km-wide dextral shear zone. This could potentially explain in part why GPS observations suggest a broad dextral shear zone spanning the SGS and the Taihang Shan (e.g., Wang & Shen, 2020; Zhang et al., 2002).

### 5.3. Implications for Geodynamics in the Shanxi Graben System

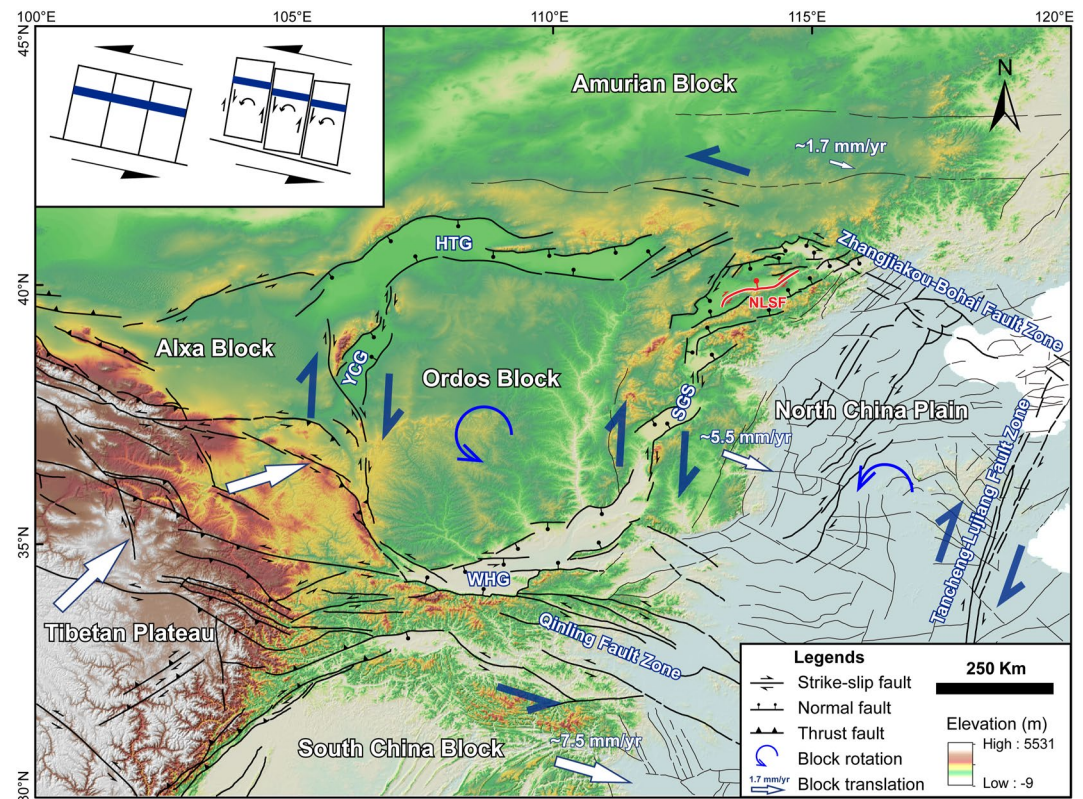
Geoscientists have long been interested in the origin and mechanism of continental rifting in the SGS (e.g., Molnar & Tapponnier, 1975; Xu & Ma, 1992; Xu et al., 1993; Ye et al., 1987). So far, there have been two end-member models proposed. The first model favors an extensional scenario, attributing the rifting in the SGS to the subduction of the Pacific Plate (Ma & Wu, 1987; Yin, 2000). Another school of thought is that the rifting is linked to the far-field effect of the India-Asia collision (e.g., Li et al., 1998; Molnar & Tapponnier, 1977; Peltzer et al., 1985; Tapponnier & Molnar, 1977; Xu & Ma, 1992; Ye et al., 1987; Zhang et al., 1998). In this model, the outward growth and expansion of the Tibetan Plateau had driven the eastward extrusion of the South China Block along the EW-striking sinistral strike-slip Qinling Fault Zone, causing counterclockwise bookshelf twisting of North China (Figure 11; Molnar & Tapponnier, 1977; Peltzer et al., 1985; Zhang et al., 1995, 1998, 2018). As a result, the SGS has evolved as a right-lateral transtensional rift system since the late Miocene (Clinkscales et al., 2020; Su et al., 2021; Xu & Ma, 1992). The first model can explain the occurrence of extension in the SGS, however, cannot explain the cause of the dextral strike-slip fault in the rift system. Thus, the direct evidence of dextral transtension in the SGS given in this study further supports the second hypothesis and therefore indicates that the evolution of the SGS is more likely driven by the outward growth of the Tibetan Plateau in response to the Cenozoic India-Eurasia collision.

### 5.4. Implications for the Crustal Deformation in North China

The pattern of deformation in North China has important implications for earthquake occurrence in that region and the broader geodynamics of East Asia. A growing body of evidence points to a “bookshelf” rotation model (e.g., England & Molnar, 1990; Freund, 1970; Mandl, 1987) for the present crustal deformation of North China (e.g., Xu & Ma, 1992; Zhang et al., 2018; Figure 11). In particular, GPS velocity fields show that eastern continental China escapes east-southeastward, with the rate gradually increasing from north to south (e.g., Shen et al., 2000; Zhang et al., 2018; Wang & Shen, 2020; Figure 11). The rapid eastward motion of the rigid South China Block (at a rate of ~7.5 mm/yr), driven by the eastward growth of the Tibetan Plateau, has resulted in a sinistral shearing over North China with respect to the slower eastward rigid Amurian Block to the north (at a rate of ~1.7 mm/yr) (Figure 11; Wang & Shen, 2020). This left-lateral shear couple between the South China Block and Amurian Block eventually led to the active deformation across North China, which is characterized by anticlockwise bookshelf rotation of the Ordos and North China Plain blocks, as well as right-lateral strike-slip along NNE-striking faults (Figure 11).

The primary NNE-striking right-lateral strike-slip fault zones in North China include the Yinchuan Graben, the SGS, and the Tancheng-Lujiang Fault Zone from west to east (Figure 11; Xu & Ma, 1992; Xu et al., 1993). The past decades have seen more and more geomorphologic and geologic evidence of dextral strike-slip in Yinchuan Graben (e.g., Liang et al., 2019; Middleton, Walker, Rood, et al., 2016) and Tancheng-Lujiang Fault Zone (e.g., Ji et al., 2021; Jiang et al., 2017), however, no further convincing evidence was documented in the SGS. Therefore, our new observations from the NLSF demonstrate the dextral strike-slip in the SGS and provide further constraints for the “bookshelf” deformation model of North China. The other way round, we tend to attribute the dextral strike-slip along the NLSF (both the western and eastern segments) and other faults in the SGS to





**Figure 11.** Topographic map showing the “bookshelf” rotation model of deformation in North China. Three main NNE (NE)-striking right-lateral strike-slip fault systems (the Yinchuan Graben fault system, Shanxi Graben System, and Tancheng-Lujiang fault zone from west to east) and two main NW (NWW)-striking left-lateral strike-slip fault systems (the Qinling fault zone in the south and Zhangjiakou-Bohai fault zone in the north) are identified in North China. The North Liulengshan Fault (NLSF) in the northern Shanxi Graben System is highlighted by a red line, while other faults are in black lines. Dark blue triangular arrows indicate the direction of relative motion. White arrows denote the block translation with respect to the stable Eurasian plate, velocity data (in  $\text{mm year}^{-1}$ ) are from Wang and Shen (2020). Inset cartoon illustrating the “bookshelf” deformation model. Abbreviations are the same as in Figure 1.

the relative motion caused by the counterclockwise rotation of the Ordos block and North China Plain block (Figure 11). After all, GPS observations show that the eastward pushing from the Tibetan Plateau at the southwestern margin of the Ordos Block makes the counterclockwise rotation of the Ordos block twice as fast as that of the North China Plain block (Wang & Shen, 2020).

## 6. Conclusion

Although the SGS has long been viewed as a dextral transtensional shear zone, the geologic and geomorphologic evidence for the dextral shearing is insufficient. The NLSF is a major active fault in the northern SGS. Its western segment has long been viewed as the main component of the dextral shear zone, which is mainly characterized by dextral strike-slip movement, while other segments of the NLSF are mainly dominated by normal faulting. However, field observations presented in this paper show that the NE-striking eastern segment of the NLSF is characterized by both right-lateral strike-slip and normal displacement. The right-lateral strike-slip component is evidenced by right-laterally offset terrace risers and stream channels as well as fault striations preserved on fault planes. Topographic surveys coupled with OSL dating of offset fluvial terraces indicate both the lateral and vertical slip rates of this fault segment are in the range of  $\sim 0.2\text{--}0.3 \text{ mm/yr}$ . The discovery of dextral strike-slip displacement along the eastern segment of the NLSF in this study provides direct and convincing evidence for determining the right-lateral transtensional kinematics of the SGS, which is of great benefit to understanding the dynamic origin of the SGS and the tectonic deformation pattern of North China.

## Data Availability Statement

The UAV survey data are archived in Mendeley Data at <https://data.mendeley.com/datasets/pkngvs92n9/1>.

## Acknowledgments

This study was jointly funded by the National Natural Science Foundation of China (41971002, U2039201) and the National Key Research and Development Program of China (2017YFC1500100). We appreciate editor Dr. Taylor Schildgen, Prof. Michael Halford Taylor at the University of Kansas, and another anonymous reviewer for their helpful comments which greatly improve the manuscript.

## References

- Ai, S. X., Zheng, Y., Riaz, M. S., Song, M. Q., Zeng, S. J., & Xie, Z. J. (2019). Seismic evidence on different rifting mechanisms in southern and northern segments of the Fenhe-Weihe Rift zone. *Journal of Geophysical Research: Solid Earth*, 124(1), 609–630. <https://doi.org/10.1029/2018JB016476>
- Allmendinger, R. W., Cardozo, N., & Fisher, D. (2012). *Structural geology algorithms: Vectors and tensors in structural geology*. Cambridge University Press.
- Bao, X. W., Song, X. D., Xu, M. J., Wang, L. S., Sun, X. X., Mi, N., et al. (2013). Crust and upper mantle structure of the North China Craton and the NE Tibetan Plateau and its tectonic implications. *Earth and Planetary Science Letters*, 369–370, 129–137. <https://doi.org/10.1016/j.epsl.2013.03.015>
- Benavente, C., Wimpenny, S., Rosell, L., Robert, X., Palomino, A., Audin, L., et al. (2021). Paleoseismic evidence of an Mw 7 pre-Hispanic earthquake in the Peruvian forearc. *Tectonics*, 40(6), e2020TC006479. <https://doi.org/10.1029/2020TC006479>
- Bi, Y. P., Pang, E. C., Sun, Y. S., Liu, Y. L., Bian, Q. M., Liu, S. Z., et al. (2022). Magnetostratigraphy of the fluvio-lacustrine sequence of core DY-1 in the Datong Basin and its implications for the evolution of the Shanxi Rift System in northern China. *Palaeogeography, Palaeoclimatology, Palaeoecology*, 599, 111063. <https://doi.org/10.1016/j.palaeo.2022.111063>
- Chen, L., Cheng, C., & Wei, Z. G. (2009). Seismic evidence for significant lateral variations in lithospheric thickness beneath the central and western North China Craton. *Earth and Planetary Science Letters*, 286(1–2), 171–183. <https://doi.org/10.1016/j.epsl.2009.06.022>
- Chen, X. Q., Chi, Z. Q., Dong, S. W., Yan, Z., Yang, J. S., Shi, W., et al. (2015). Late Cenozoic sedimentation of Nihewan Basin, central North China and its tectonic significance. *Journal of Asian Earth Sciences*, 114, 242–257. <https://doi.org/10.1016/j.jseas.2015.06.020>
- Chen, X. Q., Dong, S. W., Shi, W., Zuza, A. V., Li, Z. H., Chen, P., et al. (2021). Magnetostratigraphic ages of the Cenozoic Weihe and Shanxi Grabens in North China and their tectonic implications. *Tectonophysics*, 813, 228914. <https://doi.org/10.1016/j.tecto.2021.228914>
- Clinkscales, C., & Kapp, P. (2019). Structural style and kinematics of the Taihang-Luliangshan fold belt, North China: Implications for the Yanshanian orogeny. *Lithosphere*, 11(6), 767–783. <https://doi.org/10.1130/L1096.1>
- Clinkscales, C., Kapp, P., Thomson, S., Wang, H. Q., Laskowski, A., Orme, D. A., & Pullen, A. (2021). Regional exhumation and tectonic history of the Shanxi rift and Taihangshan, North China. *Tectonics*, 40(3), e2020TC006416. <https://doi.org/10.1029/2020TC006416>
- Clinkscales, C., Kapp, P., & Wang, H. Q. (2020). Exhumation history of the north-central Shanxi Rift, North China, revealed by low-temperature thermochronology. *Earth and Planetary Science Letters*, 536, 116146. <https://doi.org/10.1016/j.epsl.2020.116146>
- Cowgill, E. (2007). Impact of riser reconstructions on estimation of secular variation in rates of strike-slip faulting: Revisiting the Charchen River site along the Altyn Tagh Fault, NW China. *Earth and Planetary Science Letters*, 254(3–4), 239–255. <https://doi.org/10.1016/j.epsl.2006.09.015>
- Cronin, V. (2010). A primer on focal mechanism solutions for geologists. Retrieved from [http://serc.carleton.edu/files/NAGTWorkshops/structure04/Focal\\_mechanism\\_primer.pdf](http://serc.carleton.edu/files/NAGTWorkshops/structure04/Focal_mechanism_primer.pdf)
- Deng, Q., Ran, Y. K., Yang, X. P., Min, W., & Chu, Q. Z. (2007). *Active tectonics map of China (1: 4000000)*. Seismological Publishing House.
- Deng, Q. D., Cheng, S. P., Min, W., Yang, G. Z., & Ren, D. W. (1999). Discussion on Cenozoic tectonics and dynamics of Ordos block (in Chinese). *Journal of Geomechanics*, 5, 13–21.
- Deng, Q. D., Nobuyuki, Y., Xu, X. W., Suzuke, Y., Wang, C. Y., Akira, T., et al. (1994). Study on the late quaternary kinematics of the northern piedmont fault of the Liuleng Mountain (in Chinese). *Seismology and Geology*, 16, 339–343.
- Deng, Q. D., & Xu, X. W. (1995). Study on active faults and segmentation of Shanxi Graben System (in Chinese). *Research on Modern Crustal Movement*, 6, 225–241.
- Dietze, M., Kreutzer, S., Burrow, C., Fuchs, M. C., Fischer, M., & Schmidt, C. (2016). The abanico plot: Visualising chronometric data with individual standard errors. *Quaternary Geochronology*, 31, 12–18. <https://doi.org/10.1016/j.quageo.2015.09.003>
- Ding, G. Y., & Lu, Y. C. (1983). Discussion on the basic characteristics of neotectonic deformation in North China Block (in Chinese). *North China Earthquake Sciences*, 1, 1–9.
- Duan, R. T., & Fang, Z. J. (1995). Neotectonic characteristics of the northern piedmont fault of the Liuleng Mountain (in Chinese). *Seismology and Geology*, 17, 207–213.
- Duvall, A. R., & Tucker, G. E. (2015). Dynamic ridges and valleys in a strike-slip environment. *Journal of Geophysical Research: Earth Surface*, 120(10), 2016–2026. <https://doi.org/10.1002/2015JF003618>
- England, P., & Molnar, P. (1990). Right-lateral shear and rotation as the explanation for strike-slip faulting in eastern Tibet. *Nature*, 344(6262), 140–142. <https://doi.org/10.1038/344140a0>
- Freund, R. (1970). Rotation of strike-slip faults in Sistan, southeast Iran. *The Journal of Geology*, 78(2), 188–200. <https://doi.org/10.1086/627500>
- Fu, B. H., Awata, Y., Du, J. G., & He, W. G. (2005). Late Quaternary systematic stream offsets caused by repeated large seismic events along the Kunlun fault, northern Tibet. *Geomorphology*, 71(3–4), 278–292. <https://doi.org/10.1016/j.geomorph.2005.03.001>
- Galbraith, R. F., & Roberts, R. G. (2012). Statistical aspects of equivalent dose and error calculation and display in OSL dating: An overview and some recommendations. *Quaternary Geochronology*, 11, 1–27. <https://doi.org/10.1016/j.quageo.2012.04.020>
- Gao, Y., Qu, W., Zhang, Q., Chen, H. L., Liang, S. C., & Hao, M. (2022). Present-day crustal strain and major fault slip rates in North China determined using GNSS observations. *Journal of Asian Earth Sciences*, 238, 105386. <https://doi.org/10.1016/j.jseas.2022.105386>
- Gold, R. D., Briggs, R. W., Corne, A. J., & DuRoss, C. B. (2017). Refining fault slip rates using multiple displaced terrace risers—An example from the Honey Lake fault, NE California, USA. *Earth and Planetary Science Letters*, 477, 134–146. <https://doi.org/10.1016/j.epsl.2017.08.021>
- Guo, L. Q., Hu, X. K., Wang, X. W., Huang, L. R., & Zhao, W. X. (2004). Characteristics of crustal deformation and strain of Shanxi Rift Zone and seismicity (in Chinese). *Journal of Geodesy and Geodynamics*, 24, 64–71.
- Haddon, E. K., Amos, C. B., Zielke, O., Jayko, A. S., & Burgmann, R. (2016). Surface slip during large Owens Valley earthquakes. *Geochemistry, Geophysics, Geosystems*, 17(6), 2239–2269. <https://doi.org/10.1002/2015GC006033>
- Hao, M., Wang, Q. L., Zhang, P. Z., Li, Z. J., Li, Y. H., & Zhuang, W. Q. (2021). Frame wobbling” causing crustal deformation around the Ordos block. *Geophysical Research Letters*, 48(1), e2020GL091008. <https://doi.org/10.1029/2020GL091008>
- Harbert, S. A., Duvall, A. R., & Tucker, G. E. (2018). The role of near-fault relief elements in creating and maintaining a strike-slip landscape. *Geophysical Research Letters*, 45(21), 11683–11692. <https://doi.org/10.1029/2018GL080045>



- Hu, X. F., Cao, X. L., Li, T., Mao, J. W., Zhang, J., He, X., et al. (2021). Late Quaternary fault slip rate within the Qilian Orogen, insight into the deformation kinematics for the NE Tibetan Plateau. *Tectonics*, 40(5), e2020TC006586. <https://doi.org/10.1029/2020TC006586>
- Hu, X. M., Wang, L. L., Zhe, J., & Lu, H. L. (2010). Morpho-sedimentary evidence of the Huoshan Fault's late Cenozoic right-lateral movement in the Linfen Graben, Shanxi Graben system, North China. *Frontiers of Earth Science in China*, 4(3), 311–319. <https://doi.org/10.1007/s11707-010-0110-9>
- Huang, W. (1993). Morphologic patterns of stream channels on the active Yishi Fault, southern Shandong Province, eastern China: Implications for repeated great earthquakes in the Holocene. *Tectonophysics*, 219(4), 283–304. [https://doi.org/10.1016/0040-1951\(93\)90179-n](https://doi.org/10.1016/0040-1951(93)90179-n)
- Hughes, A., Rood, D. H., Whittaker, A. C., Bell, R. E., Rockwell, T. K., Levy, Y., et al. (2018). Geomorphic evidence for the geometry and slip rate of a young, low-angle thrust fault: Implications for hazard assessment and fault interaction in complex tectonic environments. *Earth and Planetary Science Letters*, 504, 198–210. <https://doi.org/10.1016/j.epsl.2018.10.003>
- Ji, H. M., Li, A., & Zhang, S. M. (2021). Analysis on the seismic characteristic displacement of Auqiu-Juxian Fault based on dextral horizontal dislocation of gully (in Chinese). *Seismology and Geology*, 43, 471–487. <https://doi.org/10.3969/j.issn.0253-4967.2021.03.001>
- Jiang, M. M., Ai, Y. S., Chen, L., & Yang, Y. J. (2013). Local modification of the lithosphere beneath the central and western North China Craton: 3-D constraints from Rayleigh wave tomography. *Gondwana Research*, 24(3–4), 849–864. <https://doi.org/10.1016/j.gr.2012.06.018>
- Jiang, W. L., Zhang, J. F., Han, Z. J., Tian, T., Jiao, Q. S., Wang, X., & Jiang, H. B. (2017). Characteristic slip of strong earthquakes along the Yishu fault zone in east China evidenced by offset landforms. *Tectonics*, 36(10), 1947–1965. <https://doi.org/10.1002/2016TC004363>
- Johnson, K., Nissen, E., Saripalli, S., Arrowsmith, J. R., McGarey, P., Schärer, K., et al. (2014). Rapid mapping of ultrafine fault zone topography with structure from motion. *Geosphere*, 10(5), 969–986. <https://doi.org/10.1130/GES01017.1>
- Kurtz, R., Klinger, Y., Ferry, M., & Ritz, J. F. (2018). Horizontal surface-slip distribution through several seismic cycles: The Eastern Bogd fault, Gobi-Altai, Mongolia. *Tectonophysics*, 734–735, 167–182. <https://doi.org/10.1016/j.tecto.2018.03.011>
- Lacassin, R., Replumaz, A., & Leloup, P. H. (1998). Hairpin river loops and slip-sense inversion on southeast Asian strike-slip faults. *Geology*, 26(8), 703–706. [https://doi.org/10.1130/0091-7613\(1998\)026<0703:hrlass>2.3.co;2](https://doi.org/10.1130/0091-7613(1998)026<0703:hrlass>2.3.co;2)
- Li, B., Kuvvet, A., Mathilde, B. S., & Jens, H. (2015). Stress pattern of the Shanxi rift system, North China, inferred from the inversion of new focal mechanisms. *Geophysical Journal International*, 201(2), 505–527. <https://doi.org/10.1093/gji/ggv025>
- Li, B., Sørensen, M. B., & Atakan, K. (2015). Coulomb stress evolution in the Shanxi rift system, North China, since 1303 associated with coseismic, post-seismic and interseismic deformation. *Geophysical Journal International*, 203(3), 1642–1664. <https://doi.org/10.1093/gji/ggv384>
- Li, C. Y., Zhang, P. Z., Yin, J. H., & Min, W. (2009). Late Quaternary left-lateral slip rate of the Haiyuan fault, northeastern margin of the Tibetan Plateau. *Tectonics*, 28(5), TC5010. <https://doi.org/10.1029/2008TC003202>
- Li, H. B., Van der Woerd, J., Tapponnier, P., Klinger, Y., Qi, X. X., Yang, J. S., & Zhu, Y. T. (2005). Slip rate on the Kunlun fault at Hongshui Gou, and recurrence time of great events comparable to the 14/11/2001, Mw~7.9 Kokoxili earthquake. *Earth and Planetary Science Letters*, 237(1–2), 285–299. <https://doi.org/10.1016/j.epsl.2005.05.041>
- Li, X., Chen, Y., Tian, X. B., & Liu, S. Z. (2022). Magnetotelluric evidence for distributed lithospheric modification beneath the Yinchuan-Jilantai rift system and its implications for Late Cenozoic rifting in western North China. *Journal of Geophysical Research: Solid Earth*, 127(3), e2021JB022585. <https://doi.org/10.1029/2021JB022585>
- Li, X. N., Li, C. Y., Pierce, I. K. D., Zhang, P. Z., Zheng, W. J., Dong, J. Y., et al. (2019). New slip rates for the Tianjingshan fault using optically stimulated luminescence, GPS, and paleoseismic data, NE Tibet, China. *Tectonophysics*, 755, 64–74. <https://doi.org/10.1016/j.tecto.2019.02.007>
- Li, X. N., Zhang, P. Z., Zheng, W. J., Feng, X. J., Li, C. Y., Pierce, I. K. D., et al. (2018). Kinematics of late quaternary slip along the Qishan-Mazhao fault: Implications for tectonic deformation on the southwestern Ordos, China. *Tectonics*, 37(9), 2983–3000. <https://doi.org/10.1029/2018TC005043>
- Li, Y. F., Liu, M., Zhang, H., & Shi, Y. L. (2021). Stream channel offsets along strike-slip faults: Interaction between fault slip and surface processes. *Geomorphology*, 394, 107965. <https://doi.org/10.1016/j.geomorph.2021.107965>
- Li, Y. H., Wang, Q. L., Cui, D. X., Hao, M., Ji, L. Y., & Qin, S. L. (2013). Research on fault motion and segmentation characteristic of Kouquan fault in Datong Basin by numerical simulation (in Chinese). *Journal of Geodesy and Geodynamics*, 33, 9–12.
- Li, Y. L., Yang, J. C., Xia, Z. K., & Mo, D. W. (1998). Tectonic geomorphology in the Shanxi Graben system, northern China. *Geomorphology*, 23(1), 77–89. [https://doi.org/10.1016/S0169-555X\(97\)00092-5](https://doi.org/10.1016/S0169-555X(97)00092-5)
- Liang, K., Ma, B. Q., Li, D. W., Tian, Q. J., Sun, C. B., He, Z. T., et al. (2019). Quaternary activity of the Zhuozishan West Piedmont Fault provides insight into the structural development of the Wuhai Basin and Northwestern Ordos block, China. *Tectonophysics*, 754, 56–72. <https://doi.org/10.1016/j.tecto.2019.02.004>
- Liu, M., Cui, X. J., & Liu, F. T. (2004). Cenozoic rifting and volcanism in eastern China: A mantle dynamic link to the Indo-Asian collision? *Tectonophysics*, 393(1–4), 29–42. <https://doi.org/10.1016/j.tecto.2004.07.029>
- Liu, R. X., Sun, J. Z., & Chen, W. J. (1983). Cenozoic basalts in North China—Their distribution, geochemical characteristics and tectonic implications. *Geochemistry*, 2(1), 17–32. <https://doi.org/10.1007/bf03180353>
- Liu, W., An, W. P., & Zhao, X. P. (1992). The 1989 Datong-Yanggao earthquake of Ms 6.1 (in Chinese). *Earthquake Research in China*, 8, 19–27.
- Lucier, A., Jong, S. M., & Turner, D. (2014). Mapping landslide displacements using Structure from Motion (SfM) and image correlation of multi-temporal UAV photography. *Progress in Physical Geography*, 38(1), 97–116. <https://doi.org/10.1177/0309133313515293>
- Luo, Q. X., Li, C. Y., Li, X. N., Ren, G. X., & Dong, J. Y. (2021). Slip distribution and footwall topography of the Yanggao-Tianzhen Fault (Northern Shanxi Graben): Implications for the along-strike variations in fault activity and regional deformation. *Tectonics*, 40(11), e2020TC006593. <https://doi.org/10.1029/2020TC006593>
- Luo, Q. X., Li, Y. L., Hu, X., Guo, A. L., Liu, Q. R., & Jiang, S. R. (2022). Constrains on the late quaternary dextral strike-slip rate of the western segment of the North Liulengshan fault in the northern Shanxi Graben system (in Chinese). *Quaternary Sciences*, 42. <https://doi.org/10.11928/j.issn.1001-7410.2022.03.08>
- Ma, X. Y., & Wu, D. N. (1987). Cenozoic extensional tectonics in China. *Tectonophysics*, 133(3–4), 243–255. [https://doi.org/10.1016/0040-1951\(87\)90268-x](https://doi.org/10.1016/0040-1951(87)90268-x)
- Mandl, G. (1987). Tectonic deformation by rotating parallel faults: The “bookshelf” mechanism. *Tectonophysics*, 141(4), 277–316. [https://doi.org/10.1016/0040-1951\(87\)90205-8](https://doi.org/10.1016/0040-1951(87)90205-8)
- Marrett, R. A., & Allmendinger, R. W. (1990). Kinematic analysis of fault-slip data. *Journal of Structural Geology*, 12(8), 973–986. [https://doi.org/10.1016/0191-8141\(90\)90093-e](https://doi.org/10.1016/0191-8141(90)90093-e)
- Middleton, T. A., Elliott, J. R., Rhodes, E. J., Sherlock, S., Walker, R. T., Wang, W. T., et al. (2017). Extension rates across the northern Shanxi Grabens, China, from Quaternary geology, seismicity and geodesy. *Geophysical Journal International*, 209, 535–558. <https://doi.org/10.1093/gji/ggx031>

- Middleton, T. A., Walker, R. T., Parsons, B., Lei, Q. Y., Zhou, Y., & Ren, Z. K. (2016). A major, intraplate, normal-faulting earthquake: The 1739 Yinchuan event in northern China. *Journal of Geophysical Research: Solid Earth*, 121(1), 293–320. <https://doi.org/10.1002/2015JB012355>
- Middleton, T. A., Walker, R. T., Rood, D. H., Rhodes, E. J., Parsons, B., Lei, Q. Y., et al. (2016). The tectonics of the western Ordos Plateau, Ningxia, China: Slip rates on the Luoshan and east Helanshan faults. *Tectonics*, 35(11), 2754–2777. <https://doi.org/10.1002/2016TC004230>
- Molnar, P., & Tapponnier, P. (1975). Cenozoic tectonics of Asia: Effects of a continental collision. *Science*, 189(4201), 419–426. <https://doi.org/10.1126/science.189.4201.419>
- Molnar, P., & Tapponnier, P. (1977). Relation of the tectonics of eastern China to the India-Eurasia collision: Application of slip-line field theory to large-scale continental tectonics. *Geology*, 5(4), 212–216. [https://doi.org/10.1130/0091-7613\(1977\)5<212:ROTTTOE>2.0.CO;2](https://doi.org/10.1130/0091-7613(1977)5<212:ROTTTOE>2.0.CO;2)
- Murray, A., Arnold, L. J., Buylaert, J. P., Guerin, g., Qin, J. T., Singhvi, A. K., et al. (2021). Optically stimulated luminescence dating using quartz. *Nature Reviews Methods Primers*, 1, 72. <https://doi.org/10.1038/s43586-021-00068-5>
- Murray, A. S., & Wintle, A. G. (2000). Luminescence dating of quartz using an improved single-aliquot regenerative-dose protocol. *Radiation Measurements*, 32(1), 57–73. [https://doi.org/10.1016/S1350-4487\(99\)00253-X](https://doi.org/10.1016/S1350-4487(99)00253-X)
- Murray, A. S., & Wintle, A. G. (2003). The single aliquot regenerative dose protocol: Potential for improvements in reliability. *Radiation Measurements*, 37(4–5), 377–381. [https://doi.org/10.1016/S1350-4487\(03\)00053-2](https://doi.org/10.1016/S1350-4487(03)00053-2)
- Northrup, C. J., Royden, L. H., & Burchfiel, B. C. (1995). Motion of the Pacific plate relative to Eurasia and its potential relation to Cenozoic extension along the eastern margin of Eurasia. *Geology*, 23(8), 719–722. [https://doi.org/10.1130/0091-7613\(1995\)023<0719:motppr>2.3.co;2](https://doi.org/10.1130/0091-7613(1995)023<0719:motppr>2.3.co;2)
- Peltzer, G., Tapponnier, P., Zhang, Z. T., & Xu, Z. Q. (1985). Neogene and quaternary faulting in and along the Qinling Shan. *Nature*, 317(6037), 500–505. <https://doi.org/10.1038/317500a0>
- Qu, W., Lu, Z., Zhang, Q., Li, Z. H., Peng, J. B., Wang, Q. L., et al. (2014). Kinematic model of crustal deformation of Fenwei basin, China based on GPS observations. *Journal of Geodynamics*, 75, 1–8. <https://doi.org/10.1016/j.jog.2014.01.001>
- Radaideh, O. M. A., & Mosar, J. (2021). Cenozoic tectonic deformation along the Pontalier strike-slip fault zone (Swiss and French Jura fold-and-thrust belt): Insights from paleostress and geomorphic analyses. *Tectonics*, 40(5), e2021TC006758. <https://doi.org/10.1029/2021TC006758>
- Reitman, N. G., Mueller, K. J., Tucker, G. E., Gold, R. D., Briggs, R. W., & Barnhart, K. R. (2019). Offset channels may not accurately record strike-slip fault displacement: Evidence from landscape evolution models. *Journal of Geophysical Research: Solid Earth*, 124(12), 13427–13451. <https://doi.org/10.1029/2019JB018596>
- Ren, J. Y., Tamaki, K., Li, S. T., & Zhang, J. X. (2002). Late Mesozoic and Cenozoic rifting and its dynamic setting in Eastern China and adjacent areas. *Tectonophysics*, 344(3–4), 175–205. [https://doi.org/10.1016/S0040-1951\(01\)00271-2](https://doi.org/10.1016/S0040-1951(01)00271-2)
- Rood, D. H., Burbank, D. W., & Finkel, R. C. (2011). Spatiotemporal patterns of fault slip rates across the Central Sierra Nevada frontal fault zone. *Earth and Planetary Science Letters*, 301(3–4), 457–468. <https://doi.org/10.1016/j.epsl.2010.11.006>
- Shen, Z. K., Zhao, C. K., Yin, A., Li, Y. X., Jackson, D. D., Fang, P., & Dong, D. A. (2000). Contemporary crustal deformation in East Asia constrained by Global Positioning System measurements. *Journal of Geophysical Research*, 105(B3), 5721–57344. <https://doi.org/10.1029/1999jb900391>
- Shi, W., Cen, M., Chen, L., Wang, Y. C., Chen, X. Q., Li, J. Y., & Chen, P. (2015). Evolution of the late Cenozoic tectonic stress regime in the Shanxi rift, central North China Plate inferred from new fault kinematic analysis. *Journal of Asian Earth Sciences*, 114, 54–72. <https://doi.org/10.1016/j.jseaes.2015.04.044>
- Sieh, K. E., & Jahns, R. H. (1984). Holocene activity of the San Andreas fault at Wallace Creek, California. *The Geological Society of America Bulletin*, 95(8), 883–896. [https://doi.org/10.1130/0016-7606\(1984\)95<883:haotsa>2.0.co;2](https://doi.org/10.1130/0016-7606(1984)95<883:haotsa>2.0.co;2)
- Song, M. Q., Zheng, Y., Ge, C., & Li, B. (2012). Relocation of small to moderate earthquakes in Shanxi Province and its relation to the seismogenic structures (in Chinese). *Chinese Journal of Geophysics*, 55, 513–525. <https://doi.org/10.6038/j.issn.0001-5733.2012.02.014>
- Song, S. W., Li, Y. H., & Hao, M. (2022). Active crustal deformation model of the Fen-Wei rift zone, North China: Integration of geologic, geodetic, and stress direction datasets. *Frontiers of Earth Science*, 10. <https://doi.org/10.3389/feart.2022.964800>
- State Seismological Bureau (SSB). (1988). *Research on active faults system around the Ordos block*. Seismological Press.
- Su, P., He, H. L., Tan, X. B., Liu, Y. D., Shi, F., & Kirby, E. (2021). Initiation and evolution of the Shanxi rift system in North China: Evidence from low-temperature thermochronology in a Plate reconstruction framework. *Tectonics*, 40(3), e2020TC006298. <https://doi.org/10.1029/2020TC006298>
- Sun, W. (2018). *Late Quaternary activity of Liuleng mountain north fault (in Chinese)*. Master's Thesis submitted to Institute of Geology, China Earthquake Administration. Retrieved from <https://chn.oversea.cnki.net/kcms/detail/detail.aspx?FileName=1018300069.nh%26DbName=CMFD2019>
- Tapponnier, P., & Molnar, P. (1977). Active faulting and tectonics in China. *Journal of Geophysical Research*, 82(20), 2906–2930. <https://doi.org/10.1029/jb082i020p02905>
- Thompson, S. C., Weldon, R. J., Rubin, C. M., Abdrakhmatov, K., Molnar, P., & Berger, G. W. (2002). Late quaternary slip rates across the central Tien Shan, Kyrgyzstan, Central Asia. *Journal of Geophysical Research*, 107(B9), 2203. <https://doi.org/10.1029/2001JB000596>
- Tian, J., & Lin, Z. (2021). Late Quaternary activity of the Qingchuan fault, eastern Tibetan Plateau margin: Insights from stream channel offsets and catchment erosion. *Geomorphology*, 395, 107949. <https://doi.org/10.1016/j.geomorph.2021.107949>
- Walker, F., & Allen, M. B. (2012). Offset rivers, drainage spacing and the record of strike-slip faulting: The Kuh Banan Fault, Iran. *Tectonophysics*, 530, 251–263. <https://doi.org/10.1016/j.tecto.2012.01.001>
- Wallace, R. E. (1949). Structure of a portion of the San Andreas rift in southern California. *The Geological Society of America Bulletin*, 60(4), 781–806. [https://doi.org/10.1130/0016-7606\(1949\)60\[781:soapot\]2.0.co;2](https://doi.org/10.1130/0016-7606(1949)60[781:soapot]2.0.co;2)
- Wallace, R. E. (1968). Notes on stream channel offset by the San Andreas fault, southern Coast Ranges, California. *Conference on geologic problems of the San Andreas fault system*, (Vol. 11, pp. 6–21). Stanford University Publication in Geological Sciences.
- Wang, H., Liu, M., Cao, J. L., Shen, X. H., & Zhang, G. M. (2011). Slip rates and seismic moment deficits on major active faults in mainland China. *Journal of Geophysical Research*, 116(B2), B02405. <https://doi.org/10.1029/2010JB007821>
- Wang, M., & Shen, Z. K. (2020). Present-day crustal deformation of continental China derived from GPS and its tectonic implications. *Journal of Geophysical Research: Solid Earth*, 125(2), e2019JB018774. <https://doi.org/10.1029/2019JB018774>
- Wang, M., & Wang, P. D. (1992). Focal mechanism and seismogenic structure of the Datong-Yanggao earthquake on October 18, 1989 (in Chinese). *Acta Seismologica Sinica*, 14, 407–415.
- Wang, N. L., Yang, J. C., Xia, Z. K., Mo, D. W., Li, Y. L., & Pan, M. (1996). *Cenozoic sedimentary and tectonic geomorphology of Shanxi Graben System (in Chinese)*. Science Publishing House.
- Wei, B. S., Wang, K., & Yao, Z. X. (1992). The 1989 Datong-Yanggao earthquake: Focal mechanisms and seismotectonic implications (in Chinese). *Earthquake Research in China*, 8, 51–59.



- Westoby, M. J., Brasington, J., Glasser, N. F., Hambrey, M. J., & Reynolds, J. M. (2012). "Structure-from-Motion" photogrammetry: A low-cost, effective tool for geoscience applications. *Geomorphology*, 179, 300–314. <https://doi.org/10.1016/j.geomorph.2012.08.021>
- Xu, W., Liu, X. D., & Zhang, S. M. (2011). Late Quaternary faulted landforms and determination of slip rates of the middle part of Kouquan fault (in Chinese). *Seismology and Geology*, 33, 335–346. <https://doi.org/10.3969/j.issn.0253-4967.2011.02.007>
- Xu, X. W., & Deng, Q. D. (1990). The features of late Quaternary activity of the piedmont fault of Mt. Huoshan, Shanxi Province and 1303 Hongdong earthquake (Ms=8) (in Chinese). *Seismology and Geology*, 12, 21–30.
- Xu, X. W., Deng, Q. D., & You, H. C. (1986). Evidence on dextral dislocation of fault at the western foothills of Mt. Xizhoushan, Shanxi Province and its slip rate during the Holocene (in Chinese). *Seismology and Geology*, 8, 44–46.
- Xu, X. W., & Ma, X. Y. (1992). Geodynamics of the Shanxi rift system, China. *Tectonophysics*, 208(1–3), 325–340. [https://doi.org/10.1016/0040-1951\(92\)90353-8](https://doi.org/10.1016/0040-1951(92)90353-8)
- Xu, X. W., Ma, X. Y., & Deng, Q. D. (1993). Neotectonic activity along the Shanxi rift system, China. *Tectonophysics*, 219(4), 305–325. [https://doi.org/10.1016/0040-1951\(93\)90180-r](https://doi.org/10.1016/0040-1951(93)90180-r)
- Xu, X. W., Ma, X. Y., Deng, Q. D., Liu, G. D., & Ma, Z. J. (1996). Neotectonics, paleoseismology and ground fissures of the Shanxi (Fenwei) rift system, China. In *30th international geological congress field trip guide T314*.
- Xu, X. W., Nobuyuki, Y., Suzuke, Y., Deng, Q. D., Wang, Y. P., Akira, T., & Wang, C. Y. (1996). Geomorphic study on late Quaternary irregular faulting along the northern piedmont of Liulengshan range, Shanxi Province, China (in Chinese). *Seismology and Geology*, 18, 169–181.
- Xu, X. W., Wu, W. M., Zhang, X. K., Ma, S. L., Ma, W. T., Yu, G. H., et al. (2002). *Recent tectonic changes and earthquakes in the crust of the Capital Area (in Chinese)*. Science Publishing House.
- Xu, Y. R. (2013). *A study on the late Quaternary faulting of the Huoshan Piedmont Fault Zone in the central Shanxi faulted basin belt (in Chinese)*. Institute of Geology, China Earthquake Administration. Beijing, Institute of Geology. Retrieved from <https://chn.oversea.cnki.net/kcms/detail.aspx?FileName=1014131207.nh%26DbName=CDFD2014>
- Xu, Y. R., He, H. L., Deng, Q. D., Allen, M. B., Sun, H. Y., & Bi, S. L. (2018). The CE 1303 Hongdong earthquake and the Huoshan Piedmont fault, Shanxi Graben: Implications for magnitude limits of normal fault earthquakes. *Journal of Geophysical Research: Solid Earth*, 123(4), 3098–3121. <https://doi.org/10.1002/2017JB014928>
- Yang, G. H., Zhao, C. K., Han, Y. P., Wang, X. W., & Guo, Y. H. (2000). Monitoring the horizontal movement along the Shanxi fault zone by GPS measurement (in Chinese). *Acta Seismologica Sinica*, 22, 465–471.
- Yang, H. B., Yang, X. P., Huang, X. N., Li, A., Huang, W. L., & Zhang, L. (2018). New constraints on slip rates of the Fodongmiao-Hongyazi fault in the Northern Qilian Shan, NE Tibet, from the 10Be exposure dating of offset terraces. *Journal of Asian Earth Sciences*, 151, 131–147. <https://doi.org/10.1016/j.jseas.2017.10.034>
- Ye, H., Zhang, B. T., & Mao, F. Y. (1987). The Cenozoic tectonic evolution of the Great North China: two types of rifting and crustal necking in the Great North China and their tectonic implications. *Tectonophysics*, 133(3–4), 217–227. [https://doi.org/10.1016/0040-1951\(87\)90265-4](https://doi.org/10.1016/0040-1951(87)90265-4)
- Yin, A. (2000). Mode of Cenozoic east-west extension in Tibet suggesting a common origin of rifts in Asia during the Indo-Asian collision. *Journal of Geophysical Research*, 105(B9), 21745–21759. <https://doi.org/10.1029/2000jb900168>
- Yin, A. (2010). Cenozoic tectonic evolution of Asia: A preliminary synthesis. *Tectonophysics*, 488(1–4), 293–325. <https://doi.org/10.1016/j.tecto.2009.06.002>
- Yin, G. M., Xu, X. W., Sun, Y. J., Chen, J., & Liu, A. G. (1997). Study on the paleoearthquake chronology of the northern piedmont fault of the Liulengshan range of Yangyuan, Hebei Province, China (in Chinese). *Earthquake Research in China*, 13, 18–26.
- Yu, J. X., Walker, R. T., Rhodes, E. J., Zhang, P. Z., Li, C. P., Wang, S. Y., et al. (2021). East Tacheng (Qoqek) Fault Zone: Late quaternary tectonics and slip rate of a left-lateral strike-slip fault zone north of the Tian Shan. *Tectonics*, 40(2), e2020TC006377. <https://doi.org/10.1029/2020TC006377>
- Yu, Z. Y., Yin, N., Wang, C. Y., Deng, M., & Lan, W. G. (2020). Active tectonics, paleoseismology and seismic hazards of the piedmont Xizhoushan fault zone in the Shanxi Graben System, North China Block. *Journal of Asian Earth Sciences*, 205, 104590. <https://doi.org/10.1016/j.jseas.2020.104590>
- Zhang, H. Q., Huang, Q. H., Zhao, G. Z., Guo, Z., & Chen, Y. J. (2016). Three-dimensional conductivity model of crust and uppermost mantle at the northern Trans North China Orogen: Evidence for a mantle source of Datong volcanoes. *Earth and Planetary Science Letters*, 453, 182–192. <https://doi.org/10.1016/j.epsl.2016.08.025>
- Zhang, P. Z., Molnar, P., & Xu, X. W. (2007). Late quaternary and present-day rates of slip along the Altyn Tagh fault, northern margin of the Tibetan Plateau. *Tectonics*, 26(5), TC5010. <https://doi.org/10.1029/2006TC002014>
- Zhang, P. Z., Wang, Q., & Ma, Z. J. (2002). GPS velocity field and active crustal blocks of contemporary tectonic deformation in continental China (in Chinese). *Earth Science Frontiers*, 9, 430–441.
- Zhang, Y. G., Zheng, W. J., Wang, Y. J., Zhang, D. L., Tian, Y. T., Wang, M., et al. (2018). Contemporary deformation of the North China Plain from Global Positioning system data. *Geophysical Research Letters*, 45(4), 1851–1859. <https://doi.org/10.1002/2017GL076599>
- Zhang, Y. Q., Mercier, J. L., & Vergely, P. (1998). Extension in the graben systems around the Ordos (China), and its contribution to the extrusion tectonics of south China with respect to Gobi-Mongolia. *Tectonophysics*, 285(1–2), 41–75. [https://doi.org/10.1016/s0040-1951\(97\)00170-4](https://doi.org/10.1016/s0040-1951(97)00170-4)
- Zhang, Y. Q., Vergely, P., & Mercier, J. (1995). Active faulting in and along the Qinling Range (China) inferred from SPOT imagery analysis and extrusion tectonics of south China. *Tectonophysics*, 243(1–2), 69–95. [https://doi.org/10.1016/0040-1951\(94\)00192-c](https://doi.org/10.1016/0040-1951(94)00192-c)
- Zhao, B., Zhang, C. H., Wang, D. Z., Huang, Y., Tan, K., Du, R. L., & Liu, J. N. (2017). Contemporary kinematics of the Ordos block, North China and its adjacent rift systems constrained by dense GPS observations. *Journal of Asian Earth Sciences*, 135, 257–267. <https://doi.org/10.1016/j.jseas.2016.12.045>
- Zhao, G. C., Sun, M., Wilde, S. A., & Li, S. Z. (2005). Late Archean to Paleoproterozoic evolution of the North China Craton: Key issues revisited. *Precambrian Research*, 136(2), 177–202. <https://doi.org/10.1016/j.precamres.2004.10.002>
- Zhu, R. X., Chen, L., Wu, F. Y., & Liu, J. L. (2011). Timing, scale and mechanism of the destruction of the North China Craton. *Science China Earth Sciences*, 54(6), 789–797. <https://doi.org/10.1007/s11430-011-4203-4>
- Zhuo, Y. Q., Guo, Y. S., Bornyakov, S. A., & Ma, J. (2019). A test of the oblique-rifting model for transfer zone deformation in the northern Fen-Wei rift: Implications from the 1989 M 6.1 Datong-Yanggao earthquake swarm. *Geodynamics & Tectonophysics*, 10(1), 43–51. <https://doi.org/10.5800/gt-2019-10-1-0403>
- Zielke, O., & Arrowsmith, J. R. (2012). LaDiCaoz and LiDARimager—MATLAB GUIs for LiDAR data handling and lateral displacement measurement. *Geosphere*, 8(1), 206–221. <https://doi.org/10.1130/GES00686.1>
- Zielke, O., Klinger, Y., & Arrowsmith, J. R. (2015). Fault slip and earthquake recurrence along strike-slip faults—Contributions of high-resolution geomorphic data. *Tectonophysics*, 638, 43–62. <https://doi.org/10.1016/j.tecto.2014.11.004>

### References From the Supporting Information

- Aitken, M. J. (1998). *An introduction to optical dating*. Oxford University Press.
- Prescott, J., & Hutton, J. (1994). Cosmic ray contributions to dose rates for luminescence and ESR dating: Large depths and long-term time variations. *Radiation Measurements*, 23(2–3), 497–500. [https://doi.org/10.1016/1350-4487\(94\)90086-8](https://doi.org/10.1016/1350-4487(94)90086-8)
- Rees-Jones, J. (1995). Optical dating of young sediments using fine-grain quartz. *Ancient TL*, 13, 9–14.